Fuel 381 (2025) 133368

Contents lists available at ScienceDirect

Fuel

journal homepage: www.elsevier.com/locate/fuel

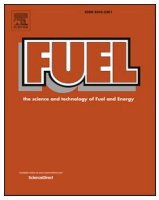

Full Length Article

Substoichiometric $La_{0.8}MnO_3$-based nanocomposites for PGM-free activation of CH_4: Ni or Cu? Surface or bulk?

Andrea Osti [a,*], Lorenzo Rizzato [a], Simone Costa [a], Jonathan Cavazzani [a], Antonella Glisenti [a,b]

[a] Department of Chemical Sciences, University of Padova, Via F. Marzolo, 1, 35131 Padova, Italy
[b] CNR-ICMATE, INSTM, Via F. Marzolo, 1, 35131 Padova, Italy

ARTICLE INFO

Keywords:
Renewable fuels
$La_{0.8}MnO_3$ perovskite
Ni, Cu doping
Ammonia deposition-precipitation
CH_4 activation

ABSTRACT

Methane is a renewable fuel when derived from biogas upgrading or by CO_2 capture and utilization, with the possibility of fully replacing natural gas in the already established gas infrastructure and engines. However, being a potent greenhouse gas, its use as fuel demands a sustainable activation procedure, to convert any residual traces of unburned CH_4 into CO_2, a challenging reaction especially at near-stoichiometric conditions typical of Three-Way Catalytic systems (TWC). To avoid expensive noble metals, we developed cheaper alternative catalysts: A-site deficient $LaMnO_3$-based nanocomposites incorporating Ni and Cu. These elements were introduced either as B-site dopants in the perovskite lattice or deposited via Ammonia-driven Deposition-Precipitation (ADP) on the perovskite surface, in both cases yielding metal nanoparticles (NPs) after a reductive treatment. Characterization encompassed various techniques: XRD, N_2 physisorption, SEM-EDX, XPS, H_2-TPR, HAADF STEM-EDX. CH_4 oxidation to CO_2 under stoichiometric O_2 served as the probe reaction, as model for TWC conditions in methane-fed engines. The LaMn-perovskite itself displayed a promising activity thanks to favourable morphological and redox features (50 % and 90 % CH_4 conversion at 581 °C and 678 °C, respectively); further improvements could be obtained upon Ni and Cu loading. The best performances were achieved by: i) the catalyst prepared by Ni-ADP (50 % and 90 % CH_4 conversion at 517 °C and 635 °C), featuring high Ni surface concentration and NPs density and a synergy with the perovskite support, as opposed to the low Ni surface concentration on B-site doped samples; ii) the reduced Cu-doped catalyst (50 % and 90 % CH_4 conversion at 508 °C and 645 °C), thanks to the high activity of reduced Cu species, the low NPs size and good metal-support interaction, in contrast to the strong NPs agglomeration of the Cu-ADP catalyst. Among the two most active catalysts, a better long-term stability was retained by the Cu-doped sample. This work laid the foundation for the development of alternative CH_4 oxidation catalysts at the stoichiometric air-to-fuel ratio, cheaper than commercial Pd-based ones.

1. Introduction

Methane is one of the relevant candidate renewable fuels for supporting the energy transition: the anaerobic digestion of biomass wastes through specialized bacteria yields biogas, which is essentially a mixture of CH_4 and CO_2 (and other traces components) and can be further purified to obtain biomethane. As such, it can replace natural gas in the already established pipelines and engines, without any technological modifications [1,2]. Moreover, CH_4 is a versatile energy and hydrogen vector that can be employed for heating generation on both residential and industrial sectors, as fuel in internal combustion engines or fuel cells (directly in Solid Oxide Fuel Cells, as an example, after reforming in all fuel cells) [3]. Also in traditional engines, methane has some advantages compared to gasoline and diesel, such as a lower fuel price and lower emission of pollutants CO_2, NO_x and particulate matter (PM) [4]. However, CH_4 is a powerful greenhouse gas, with a global warming potential ~25 times higher than CO_2 [5]; consequently, traces of unburned methane from engines exhaust must be removed to avoid an environmentally detrimental effect. The high stability of this molecule (C–H bond energy 439.3 kJ/mol [6]) induces the use of catalysts characterized by high loading of Platinum group metals (PGMs) to accomplish the total CH_4 oxidation (besides CO oxidation and NO_x reduction), for which Pd is recognized as the most active metal [4,7]. A sustainable use of CH_4 as transition fuel, requires the development of cheaper PGM-

* Corresponding author.
E-mail address: andrea.osti.1@phd.unipd.it (A. Osti).

https://doi.org/10.1016/j.fuel.2024.133368
Received 9 April 2024; Received in revised form 30 September 2024; Accepted 2 October 2024
Available online 5 October 2024

free activation catalysts: with this aim, alternative formulations based on Cu and Ni have been developed and compared in the present manuscript. Cu-based catalysts have been studied, as an example, for engines aftertreatment technologies, highlighting their activity in CO oxidation, hydrocarbons (C_{3+}) oxidation and NO reduction [8]. Concerning CH_4 combustion (mainly in lean conditions, i.e., in excess of O_2), CuO-based catalysts have been investigated by some researchers showing promising performances [9–11]. Ni-based catalysts have also been identified as being more active (in lean conditions) than Fe_2O_3 and Co_3O_4 [12]. Synergistic effect between metal and support in CH_4 oxidation have been reported for NiO/CeO_2 or $NiO/Ce_{1-x}Zr_xO_2$ catalysts [13–15]. It was also shown that NiO/CeO_2 was able to catalyse the NO reduction assisted by CO [16]. These results pointed out that Ni- and Cu-based catalysts could be good candidates to activate CH_4 as well as the other reactions involved in Three-Way Catalytic systems (TWC).

To exploit the catalytic activity of these two metals they need to be highly dispersed on a support and, to reach the expected result, a support capable of contributing to the catalytic activity is to be preferred. Perovskite oxides, with general formula ABO_3, have been widely investigated in the past decades as catalysts in several oxidation and reduction reactions, among those CH_4 oxidation, especially compositions based on $LaBO_3$ (B = Mn, Fe, Co) [6,17]. The transition metal at B-site possesses redox capabilities, while the A-site element La is known to confer structural stability and a good resistance to harsh thermal conditions, like those typical of engines after-treatment technologies, as an example. Such materials also display oxygen storage capacity (OSC), similarly to the more widespread CeO_2, i.e., the ability to reversibly adsorb and release oxygen to balance the oscillating reducing-oxidizing conditions typical of TWC gas mixtures [18,19]. For these reasons, $LaBO_3$-derived perovskites have been greatly investigated as possible alternatives to PGMs for exhausts treatment, or as support for other metal/metal oxides as CuO [20–26]. In particular, $LaMnO_3$ and $LaCoO_3$-based perovskites are generally more active than $LaFeO_3$ in CH_4 oxidation [27,28], but the long-term stability of $LaMnO_3$ is usually higher than that of $LaCoO_3$ [29], as well as the stability in reducing conditions. For these reasons, Mn-perovskites have been considered in this work.

The dissociation and subsequent oxidation of CH_4 over perovskites is reported to involve active oxygen species coming from the oxide catalyst: weakly adsorbed oxygen species at lower temperatures (suprafacial mechanism), lattice oxygen species coming from the surface and subsurface layers at higher temperatures (intrafacial mechanism) [17,30,31]. This mechanism is often described as a Mars-Van Krevelen (MvK) type [32–34], involving reduction–oxidation cycles of the active sites: the loss of active oxygen species (attacking adsorbed CH_4 and CH_x fragments) results in the formation of oxygen vacancies (V_O) and in the reduction of surface sites (B-site cations), which are then re-oxidized by the adsorption of gas phase O_2, replenishing V_O. Therefore, besides the number of active sites and thus the exposed surface area, other factors affecting catalytic activity towards CH_4 combustion are the ease of oxygen release from perovskite surface and subsurface layers and the presence of highly reducible transition metal cations at surface, being reducibility connected to the release of active oxygen species [33–37]. Hence, a widely explored strategy to boost oxidation activity of perovskites is to create charge imbalances at A-site, either through the introduction of aliovalent dopants (e.g., Sr^{2+}, Ca^{2+} replacing some La^{3+}) [35,38,39] or through a La-deficient composition [40–42]. In these ways, to compensate the missing positive charges at A-site, a fraction of B-site cations can be overoxidized or a higher number of V_O can be generated, with the consequence of enhancing surface and/or lattice oxygen mobility and B-site cation reducibility. Moreover, the substoichiometry is of some help in minimizing the stable formation of surface carbonate species that can poison the catalyst. The introduction of a second transition metal cation at B-site, including Ni and Cu, was also reported to favour hydrocarbon oxidation activity thanks to improved surface area, reducibility and surface oxygen mobility [43,44].

Another consideration this contribute is based on, is the use of $LaBO_3$ compositions as precursors for obtaining surface segregated metal nanoparticles (NPs), supported over the perovskite oxide [45–49]. It was shown that, when doped at the B-site, Pd and other PGMs species can reversibly segregate outside the oxide lattice in reducing conditions to form well dispersed metal NPs, then be reincorporated inside the hosting matrix in oxidizing conditions, thus avoiding sintering and loss of active sites [50]. A similar protection and recovery mechanism was demonstrated for other reducible metals as well, like Ni and Cu, when doped at the B-site [44,51]. The process of metal particle segregation in reducing conditions, called exsolution, is favoured by A-site cation deficiency [52]. Even when supporting an active metal like Pd, La_xMnO_3 perovskites can assist the activation of CH_4 by providing active oxygen species at the interface with Pd particles, especially with La-deficient compositions ($x < 1$) [53]. An analogous beneficial effect of the support providing active oxygen species, was reported for NiO/CeO_2 catalysts at the Ni-O-Ce interfacial sites, through a similar MvK mechanism [54].

Based on the abovementioned considerations, in this work $La_{0.8}MnO_3$ perovskite oxides, functionalized with Ni and Cu, were implemented for the total oxidation of CH_4 to CO_2 in a stoichiometric reaction mixture. Indeed, most of the previous works investigating alternative CH_4 oxidation catalysts (PGM-free) carried out the reaction under excess of O_2 [55], while there is still a lack of research focusing on CH_4 combustion around the stoichiometric point, typical of TWC systems applied to methane fed-engines. Two strategies were exploited for metal loading on perovskite and compared: i) exsolution from perovskite doped at B-site; ii) Ammonia-driven deposition precipitation (ADP). In the first case, the metal NPs grow on the support surface coming from inside the support, and the so-called matrix socket can protect them from coalescence, but the amount that can be deposited on the surface depends on the solubility of Ni, or Cu, into the lattice [56]. In the second case the procedure allows to deposit the desired amount of metal NPs, but they can growth with time and temperature. In ADP procedure, developed by Guo et al. [57] and optimized for perovskites [25], a more uniform particle distribution with respect to common wet impregnation is warranted by the formation of NH_3-metal complexes during synthesis. The prepared catalysts were well characterized by several techniques (XRD, H_2-TPR, N_2 physisorption, XPS, SEM-EDX, HAADF STEM-EDX) and subjected to a reductive treatment to yield Ni^0 and Cu^0 NPs supported on perovskite. Both calcined and reduced catalysts were tested for CH_4 combustion; differences in catalytic activity depending on the kind of metal, synthesis protocol and catalyst pre-treatment were correlated with the results of physicochemical characterizations. To the best of our knowledge, this is the first work on Ni- and Cu-catalysts supported on La_xMnO_3 perovskite purposedly designed for CH_4 combustion in stoichiometric conditions. The obtained results allowed a global understanding of the effect of surface composition, metal NPs-perovskite interface, and metal NPs morphology on catalytic activity in CH_4 activation.

2. Experimental

2.1. Synthesis of catalysts

The reference perovskite of composition $La_{0.8}MnO_3$ was synthesized by the sol–gel citrate combustion method, based on an optimized procedure object of a previous study [58]. Briefly, metal precursors La_2O_3 ($\geq$ 99.9 % Sigma-Aldrich) and $Mn(CH_3COO)_2$ tetrahydrate ($\geq$99 % Sigma-Aldrich) were dissolved in water + HNO_3 ($\geq$ 65 % Sigma-Aldrich) (pH < 1); citric acid monohydrate (CA, $\geq$ 99.0 % Sigma-Aldrich) was added according to a molar ratio CA/metal cations of 1.1. After gel formation and decomposition at 200–230 °C for 1 h, the final perovskite was obtained upon calcination in air at 750 °C for 6 h.

Ni- and Cu-loading were performed either as one-step B-site doping of the perovskite lattice, by adding Ni or Cu precursors (respectively, Ni

$(NO_3)_2$ hexahydrate ≥ 97.0 % Sigma-Aldrich and CuO ≥ 99.0 % Sigma-Aldrich) in the sol–gel solution, or by a two-step Ammonia-driven Deposition Precipitation (ADP) [23]. In the former case, the nominal perovskite compositions were $La_{0.8}Mn_{0.9}Ni_{0.1}O_3$, $La_{0.8}Mn_{0.9}Cu_{0.1}O_3$ and $La_{0.8}Mn_{0.8}Ni_{0.2}O_3$. In the latter case, the calcined $La_{0.8}MnO_3$ powder (~ 1.5 g) was impregnated with an aqueous solution of $Ni(NO_3)_2$ hexahydrate or $Cu(NO_3)_2$ trihydrate (puriss. 99–104 % Sigma-Aldrich), then NH_3 (32 % Sigma-Aldrich) was added as complexing agent with a molar ratio NH_3/metal = 6:1 by stirring overnight. The solvent was subsequently evaporated at 120 °C for 2 h, and the resulting powder was calcined in air at 550 °C for 6 h, to obtain NiO/$La_{0.8}MnO_3$ and CuO/$La_{0.8}MnO_3$. The amount of Ni and Cu deposited through ADP was equivalent to 0.2 B-site doping.

A fraction of each catalyst (~ 100 mg), loaded in a fix bed quartz reactor between two plugs of quartz wool, was reduced in 100 cm^3/min STP of 2 vol% H_2/Ar for 2 h, at a temperature determined by H_2-TPR: 400 °C for Cu-containing samples, 590–650 °C for Ni-containing samples; the reference $La_{0.8}MnO_3$ was also reduced at 400 and at 650 °C for comparison purposes.

The list of all the prepared catalyst samples and their synthesis procedures is reported in Table 1.

2.2. Characterizations

Powder X-ray diffraction (XRD) patterns were acquired with a Bruker D8 Advanced diffractometer in Bragg-Brentano geometry, employing a Cu Kα source (λ = 1.5406 Å), powered at 40 kV and 40 mA, with steps of 0.02° and dwell time 0.35 s/step. Average perovskites crystallite size was estimated with the Williamson-Hall method by fitting three reflections at 2θ = 22.9°, 32.5° or 32.8°, 46.8° (lattice planes (0 1 2), (1 1 0) or (1 0 4), (0 2 4), respectively).

Additionally, for the three B-site doped freshly calcined catalysts, high-resolution XRD patterns were collected at the ID22 Beamline of the ESRF, in the 2θ range 0-130° with wavelength λ = 0.354408 Å. The samples were pressed into 0.7 mm Kapton capillaries to optimize transmission and analysed at RT.

N_2 adsorption isotherms were collected at −196 °C with a Micromeritics ASAP2020 Plus instrument, in the relative pressure range (p/p^0) 0.01–1.0 and vice versa; prior to experiments, the samples (0.5–1 g) were outgassed in vacuum (p < 1.3 Pa) at 300 °C for 3 h. Specific surface areas (SSA) were determined according to Brunauer-Emmett-Teller (BET) model, and pore size distributions according to Barrett-Joyner-Halenda (BJH) model.

H_2-Temperature programmed reduction (TPR) was carried out to investigate the materials reducibility, on a Micromeritics Autochem II 2920 apparatus. 50 mg of sample were loaded in a U-shaped quartz reactor, above a layer of quartz wool, and heated from RT to 950 °C (ramp 10 °C/min) under a 50 cm^3/min STP flow of 5 % H_2/Ar. The H_2 consumption was monitored with a TCD detector after H_2O absorption by a cold trap.

Table 1
List of the prepared catalysts and their respective synthesis conditions.

Sample	Synthesis method	Last thermal treatment
$La_{0.8}MnO_3$ fresh	Citrate combustion	Calcination in air, 750 °C, 6 h
$La_{0.8}Mn_{0.9}Ni_{0.1}O_3$ fresh	Citrate combustion	Calcination in air, 750 °C, 6 h
$La_{0.8}Mn_{0.9}Cu_{0.1}O_3$ fresh	Citrate combustion	Calcination in air, 750 °C, 6 h
$La_{0.8}Mn_{0.8}Ni_{0.2}O_3$ fresh	Citrate combustion	Calcination in air, 750 °C, 6 h
$Ni_{0.2}/La_{0.8}MnO_3$ fresh	Ammonia dep.-prec.	Calcination in air, 550 °C, 6 h
$Cu_{0.2}/La_{0.8}MnO_3$ fresh	Ammonia dep.-prec.	Calcination in air, 550 °C, 6 h
$La_{0.8}MnO_3$ r400	Citrate combustion	Reduction in 2 % H_2, 400 °C, 2 h
$La_{0.8}MnO_3$ r650	Citrate combustion	Reduction in 2 % H_2, 650 °C, 2 h
$La_{0.8}Mn_{0.9}Ni_{0.1}O_3$ r650	Citrate combustion	Reduction in 2 % H_2, 650 °C, 2 h
$La_{0.8}Mn_{0.9}Cu_{0.1}O_3$ r400	Citrate combustion	Reduction in 2 % H_2, 400 °C, 2 h
$La_{0.8}Mn_{0.8}Ni_{0.2}O_3$ r620	Citrate combustion	Reduction in 2 % H_2, 620 °C, 2 h
$Ni_{0.2}/La_{0.8}MnO_3$ r590	Ammonia dep.-prec.	Reduction in 2 % H_2, 590 °C, 2 h
$Cu_{0.2}/La_{0.8}MnO_3$ r400	Ammonia dep.-prec.	Reduction in 2 % H_2, 400 °C, 2 h

Scanning electron microscopy (SEM) images were acquired with a Zeiss SUPRA 40 V P microscope, setting the electron acceleration voltage at 5 to 20 kV. Energy-dispersive X-ray analysis (EDX) was coupled to SEM for elemental quantification, at 20 kV electron acceleration voltage, probing a large area of sample (rectangle of hundreds of μm each side); X-ray peaks considered for quantification were O Kα, Mn Kα, La Lα, Ni Kα and Cu Kα.

X-ray photoelectron spectroscopy (XPS) was performed with a Thermo Scientific ESCALAB QXi spectrometer, employing a monochromatized Al Kα source (hν = 1486.68 eV) and a charge compensation gun. The spectrometer was calibrated by assuming the binding energy (BE) of the Au $4f_{7/2}$ line to be 84.0 eV with respect to the Fermi level. Survey spectra were acquired at pass energy 100 eV, 0.5 eV/step and dwell time 25 ms/step; detailed spectra on C 1s, O 1s, La 3d + Ni 2p (partially overlapping), Mn 2p, O 1s, Ni 3p and Cu 2p photopeaks were acquired at pass energy 20 eV, 0.1 eV/step and dwell time 25 ms/step. The charging problem has been afforded by means of the charge compensation gun and moreover, setting the adventitious carbon C 1s peak at 284.8 eV. Elemental quantification was carried by integration of La $3d_{5/2}$, Mn 2p, O 1s, Ni 3p and Cu 2p photopeaks, after Shirley-type background subtraction. Peaks deconvolution was performed by assuming a mixed Lorentzian/Gaussian 30/70 shape.

Scanning transmission electron microscopy (STEM) was performed on Ni- and Cu-containing samples after undergoing reduction in 2 vol% H_2/Ar, with a JEOL JEM-F200 microscope operating at 200 kV. A high angle annular dark field (HAADF) detector was used for morphological imaging, coupled with a EDX detector for elemental mapping. The sample preparation procedure consisted in dispersing the powder in ethanol (99 %) by ultrasonication and in the deposition of few drops of the dispersion on a carbon-coated Au grid.

2.3. Catalytic tests

The prepared catalysts were tested for CH_4 complete oxidation to CO_2 under stoichiometric O_2. A fix bed quartz reactor (ID 6 mm) was employed, loading 50 mg of sample between two layers of quartz wool, and a K-type thermocouple was placed upstream of the catalyst bed to monitor its temperature. The reaction mixture was composed of 2 vol% CH_4, 4 vol% O_2, 16 vol% N_2 and He balance, with total flow rate 100 cm^3/min STP (weighted hourly space velocity, WHSV = 120 L/h/g). The light-off CH_4 conversion tests were conducted in the temperature range 300–800 °C by heating up at 2 °C/min. Stability tests on selected samples were carried out by stationing for 18 h at 600 °C inside the reaction mixture, after an analogous heating stage at 2 °C/min. The catalysts were tested either freshly calcined without any pretreatment, or after an in-situ reduction under 2 vol% H_2/Ar (100 cm^3/min STP) for 2 h, at the temperature necessary to reduce Ni^{2+}/Cu^{2+} to the metallic state, as determined by H_2-TPR. The outlet gas mixture was analysed by an on-line GC (Agilent 7890A), equipped with a TCD detector and two packed columns, MolSieve 13X (60/80 mesh, 1.8 m) and Porapak Q (80/100 mesh, 1.8 m), using He as carrier gas.

Reaction rates of CH_4 conversion were calculated assuming the mass balance of a plug flow reactor (PFR) and a first order kinetics with respect to methane concentration, leading to the following Eq. (1) and Eq. (2) for the specific rate ($r_{specific}$, normalized by catalyst mass) and intrinsic rate ($r_{intrinsic}$, normalized by catalyst surface area), respectively [20].

$$r_{specific} = \frac{F_{CH4,0}}{m}(1 - X_{CH4})\ln\frac{1}{1 - X_{CH4}}(\mathrm{mol/s/g}). \quad (1)$$

$$r_{intrinsic} = r_{specific}/SSA(\mathrm{mol/s/m^2}). \quad (2)$$

X_{CH4} is the methane conversion, m the catalyst mass (g), $F_{CH4,0}$ the inlet molar flow rate of methane (mol/s) and SSA the catalyst specific surface area (m^2/g) as determined from BET method. In turn, the methane conversion was calculated by equation (3), where $C_{CH4,0}$ is the

inlet concentration (2 vol%) and $C_{CH4,T}$ the outlet concentration at a certain temperature, as quantified by GC.

$$X_{CH4} = \frac{C_{CH4,0} - C_{CH4,T}}{C_{CH4,0}} \quad (3)$$

3. Results and discussion

3.1. Structural and morphological features

XRD patterns of the freshly calcined perovskites are shown in Fig. 1. In all cases, the main observed phase was hexagonal $La_{0.887}MnO_3$ (space group R-3c:H, COD reference 1531294), without variations after Ni- and Cu-loading. The hexagonal/rhombohedral $LaMnO_3$-like phases are known to possess a mixture of Mn^{3+} and Mn^{4+} in the lattice, coupled with a defect of both A- and B-site cations with respect to O^{2-} anions [17,31]. Isolated MnO_x species were not detected as a result of A-site deficiency, although they might be amorphous or very well dispersed on the perovskite surface, as suggested in other works [40,42]. Ni^{2+} seemed completely incorporated in the perovskite lattice when 10 mol% doping at B-site was performed, whereas a weak NiO reflection at $2\theta = 43.4°$ was probably detected at higher doping amount, 20 mol%, indicating an uncomplete inclusion in the oxide matrix. A similar uncomplete inclusion of Cu^{2+} was suggested even for the Cu B-site doped sample, since a weak reflection ascribed to $CuMn_2O_4$ spinel seemed to be present at $2\theta = 36.0°$. For ADP samples, weak reflections ascribed to NiO ($2\theta = 43.4°$) or CuO ($2\theta = 35.6°$ and $38.8°$) were spotted besides the main perovskite phase, likely confirming the deposition of oxide NPs on the surface of $La_{0.8}MnO_3$ support.

To further confirm the presence/absence of Ni- and Cu-containing phases in B-site doped samples, high resolution XRD was performed at ID22 beamline of ESRF, with an incident wavelength of 0.354408 Å. The resulting diffractograms are reported in Figure S1. For $La_{0.8}Mn_{0.9}Ni_{0.1}O_3$, no other phases except the main perovskite could be detected, likely confirming the complete Ni incorporation in the lattice. For $La_{0.8}Mn_{0.9}Cu_{0.1}O_3$, the presence of impurities of $CuMn_2O_4$ spinel were confirmed; besides, even weaker impurities of a Ruddlesden-Popper La_2CuO_4 phase and of $La(OH)_3$ could be detected for the first time. Globally, it is evident that Cu^{2+} was not completely incorporated in the perovskite framework even at 10 mol% doping; the reason could be the size mismatch with respect to the main Mn^{3+} cation (Cu^{2+} 0.87 Å vs. Mn^{3+} 0.785 Å), which is higher than in the case of Ni-doping (Ni^{2+} 0.83 Å) [59]. Finally, for $La_{0.8}Mn_{0.8}Ni_{0.2}O_3$ the presence of a weak NiO phase was confirmed, and an additionally weak impurity of $NiMn_2O_4$ spinel phase was also spotted. Hence, a lattice inclusion of Ni lower than the theoretical value of 0.2, but probably higher than 0.1, was confirmed.

The average crystallite size of the main perovskite phase was

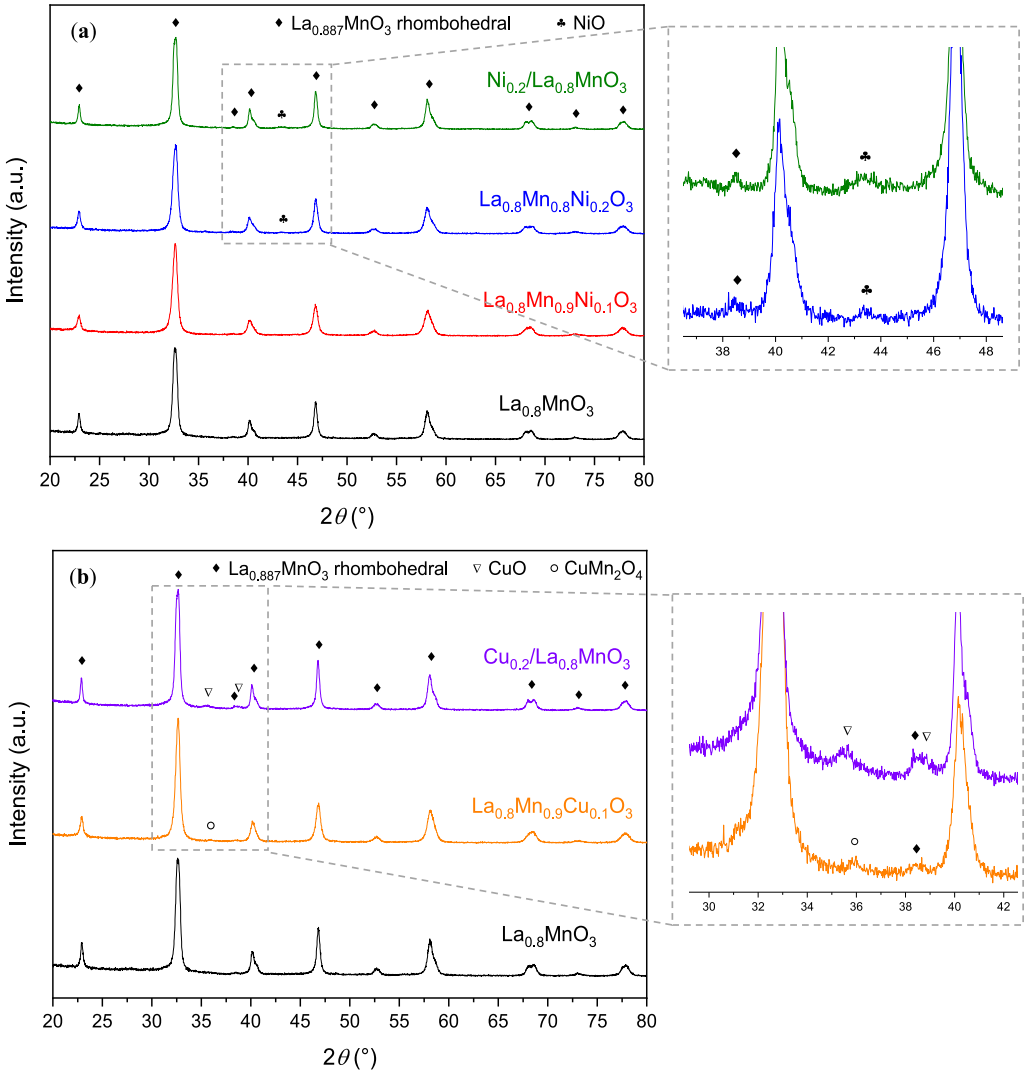

Fig. 1. XRD patterns of the calcined perovskites: (**a**) Ni-containing samples, compared to the reference $La_{0.8}MnO_3$, with zoom on the region were NiO reflections are spotted; (**b**) Cu-containing samples, compared to the reference $La_{0.8}MnO_3$, with zoom on the region were CuO and $CuMn_2O_4$ reflections are spotted.

extracted from XRD patterns through the Williamson-Hall method; the results are reported in Table 2. It appears that B-site doping by either Ni or Cu cations tends to decrease the average size compared to the reference $La_{0.8}MnO_3$ composition, whereas a slight increase was observed after Ni- and Cu-ADP, probably due to the additional thermal treatment performed in the latter case. These results mostly agree with surface areas and pore volumes obtained from N_2 physisorption isotherms, also listed in Table 2, showing that a decrease in crystallite size is accompanied by an expected increase in the surface area and total porosity. In particular, the mesoporosity is enhanced in B-site doped compositions compared to benchmark $La_{0.8}MnO_3$, as shown from the broader hysteresis loops of N_2 isotherms and by the BJH pore size distribution (Figure S2). Such morphological improvements could be related to the unit cell distortion and creation of defects arising from dopant incorporation rather than on the difference in the gel thermal decomposition, as discussed in more details in our previous work [58]. The SSA and porosity values of $Cu_{0.2}/La_{0.8}MnO_3$ prepared by ADP were slightly decreased compared to the bare support, in agreement with the higher XRD crystallite size, whereas a (counterintuitive) slight increase in SSA was observed for $Ni_{0.2}/La_{0.8}MnO_3$, which could be explained by the deposition of relatively small NiO NPs contributing to the total surface area. In any case, the adsorption isotherm and pore size distribution of both ADP samples (Figure S2) were very similar to those of the reference $La_{0.8}MnO_3$, in agreement with a surface deposition of metal oxide particles without significant alteration of the underlying support morphology.

XRD patterns of the samples subjected to a reductive treatment under 2 vol% H_2/Ar are shown in Fig. 2 and Figure S3, compared to the pattern of freshly calcined $La_{0.8}MnO_3$ as reference. In all cases, the principal perovskite phase was modified from the original rhombohedral to the new orthorhombic symmetry, explained by the reduction of Mn^{4+} ions to Mn^{3+} (see also H_2-TPR) which expands the unit cell and shifts the reflections towards lower angles, characteristic of the orthorhombic phase (Figure S3). Importantly, despite the structural modification, the perovskite structure was preserved, apart from minor signs of MnO formation on some samples, e.g., $Ni_{0.2}/La_{0.8}MnO_3$ reduced at 590 °C; the necessity of maintaining the perovskite phase even after the reduction was the main reason for the choice of a very diluted H_2 atmosphere, since a higher concentration of H_2 would have risked to further reduce Mn species to the +2 state, not compatible with the perovskite structure. Additionally, Ni^{2+} seemed successfully reduced to the metallic state by detection of a weak reflection ascribed to Ni^0 at $2\theta = 44.5°$, surely for the samples with higher Ni-content ($La_{0.8}Mn_{0.8}Ni_{0.2}O_3$ and $Ni_{0.2}/La_{0.8}MnO_3$), less evident but likely present in the sample $La_{0.8}Mn_{0.9}Ni_{0.1}O_3$. Similarly, a reflection ascribed to Cu^0 was detected at $2\theta = 43.3°$ on sample $Cu_{0.2}/La_{0.8}MnO_3$ after the reductive treatment, whereas it was not evident for the sample with lower Cu-content, i.e., $La_{0.8}Mn_{0.9}Cu_{0.1}O_3$. In general, the formation of Ni^0 or Cu^0 NPs, primary goal of the reductive treatment, seemed confirmed by XRD.

Representative SEM micrographs of the freshly calcined and reduced perovskites are displayed in Fig. 3 and Figure S4. In general, the samples are characterized by aggregates of small crystal grains, with size in the range of tens of nm as roughly estimated from XRD patterns. Freshly calcined B-site doped samples (Fig. 3a, S4b, S4d) possess a looser morphology and the presence of more abundant meso/macropores compared to benchmark $La_{0.8}MnO_3$ (Fig. S3a) and to ADP samples (Fig. 3c and S4f), in agreement with N_2 sorption analysis. In turn, the latter are characterized by a more compact morphology, probably because of the additional thermal treatment to deposit NiO and CuO particles. Samples subjected to a reductive treatment (Fig. 3b, 3d, S4c, S4e, S4g) generally show some signs of aggregation compared to the respective fresh counterparts, but small grains and a certain porosity seem well maintained, especially in B-site doped compositions (Fig. 3b, S4c, S4e).

Table 2
Morphological features of the six calcined perovskites: specific surface area (SSA), total pore volume and average crystallite size (d_{XRD}).

Sample	SSA (m^2/g) [1]	Pore Vol. (cm^3/g) [2]	d_{XRD} (nm) [3]
$La_{0.8}MnO_3$	25.0	0.187	33.1
$La_{0.8}Mn_{0.9}Ni_{0.1}O_3$	43.9	0.287	22.7
$La_{0.8}Mn_{0.9}Cu_{0.1}O_3$	37.1	0.281	32.2
$La_{0.8}Mn_{0.8}Ni_{0.2}O_3$	38.0	0.252	24.7
$Ni_{0.2}/La_{0.8}MnO_3$	28.2	0.183	35.9
$Cu_{0.2}/La_{0.8}MnO_3$	23.2	0.137	41.4

[1] Determined by BET method.
[2] Determined by BJH method.
[3] Determined by Williamson–Hall method, with K=0.90 and λ = 0.154 nm.

3.2. Bulk reducibility

Samples reducibility was evaluated by H_2-TPR. The recorded profiles are reported in Fig. 4, and reduction temperatures and quantification of H_2 consumption are listed in Table 3. Two main reduction processes are discernible on all the prepared catalysts: $Mn^{4+} \rightarrow Mn^{3+}$ reduction in the lower temperature range (150–500 °C), in parallel with the removal of the excessive lattice oxygen with respect to metal cations, and $Mn^{3+} \rightarrow Mn^{2+}$ reduction in the higher temperature range (600–850 °C), leading to perovskite decomposition into simple oxides/hydroxides (La_2O_3 or $La(OH)_3$ + MnO) [30,40]. The high H_2 consumption in the low temperature range for $La_{0.8}MnO_3$ reflects a high amount of Mn^{4+} stabilized in the structure, probably needed to compensate the charge imbalance created by A-site deficiency as well as by the oxygen excess usually observed on $LaMnO_{3+\delta}$ perovskites [17,37].

Furthermore, the low-temperature shoulder at 200–250 °C, enhanced on Ni B-site doped samples (Fig. 4a), could be attributed to the reduction of highly reducible Mn^{4+} species located at the abundant surface or pore sites, which are indeed more numerous after Ni-doping, as revealed by N_2 physisorption. The effect of Ni-loading can be appreciated on $Ni_{0.2}/La_{0.8}MnO_3$ sample, since two new peaks in the range 400–600 °C appeared, ascribed to the reduction of NiO to metallic Ni [60], as verified by the detection of Ni^0 on the XRD pattern after reduction at 590 °C; no significant modification of the other reduction processes ascribed to Mn ions could be noticed, in agreement with a surface deposition not affecting the perovskite support. On the other hand, the reduction of Ni^{2+} species on B-site doped samples was not clearly visible on the TPR profiles and may fall around 600–650 °C, as previously found in literature for similar compositions [60], thus hidden by the rising part of the Mn^{3+} reduction peak; this was confirmed by the detection of some metallic Ni on the XRD patterns of $La_{0.8}Mn_{0.9}Ni_{0.1}O_3$ and $La_{0.8}Mn_{0.8}Ni_{0.2}O_3$ reduced at 650 and 620 °C, respectively. Contrarily to ADP, Ni doping at B-site modified the perovskite lattice reducibility [43,60], anticipating the Mn^{4+} reduction peak by 30–50 °C with respect to the benchmark $La_{0.8}MnO_3$ and shifting Mn^{3+} reduction towards lower temperatures as well, especially for $La_{0.8}Mn_{0.8}Ni_{0.2}O_3$. Thus, despite the detection of a NiO phase by XRD on this latter (fresh) sample, the improvement of perovskite reducibility indicates a major Ni^{2+} inclusion as dopant ion. Ni-doping also attenuated the amount of Mn^{4+} stabilized in the perovskite lattice in favour of Mn^{3+}, as indicated by the higher H_2 consumption in the high temperature region at the expense of the low temperature one, as previously found in the literature [61]. The effect of Cu loading, either as (partial) B-site doping or as ADP (Fig. 4b), is evident in the low temperature region: two shoulders in the range 100–220 °C appeared on the TPR profile, assigned to the successive $Cu^{2+} \rightarrow Cu^{+}$ and $Cu^{+} \rightarrow Cu^0$ reduction events [44]. For $La_{0.8}Mn_{0.9}Cu_{0.1}O_3$, in fact, these peaks may be ascribed to the reduction of impurity Cu-containing phases (La_2CuO_4 and $CuMn_2O_4$), as another small peak centred at 335 °C could be assigned to the reduction by exsolution of Cu^{2+} ions truly stabilized inside the perovskite lattice, a peak not observed when CuO was deposited by ADP. Furthermore, Mn^{4+} reduction was greatly anticipated (of about 100 °C) compared to benchmark $La_{0.8}MnO_3$, thanks to the effect of H_2 spillover: once Cu^0

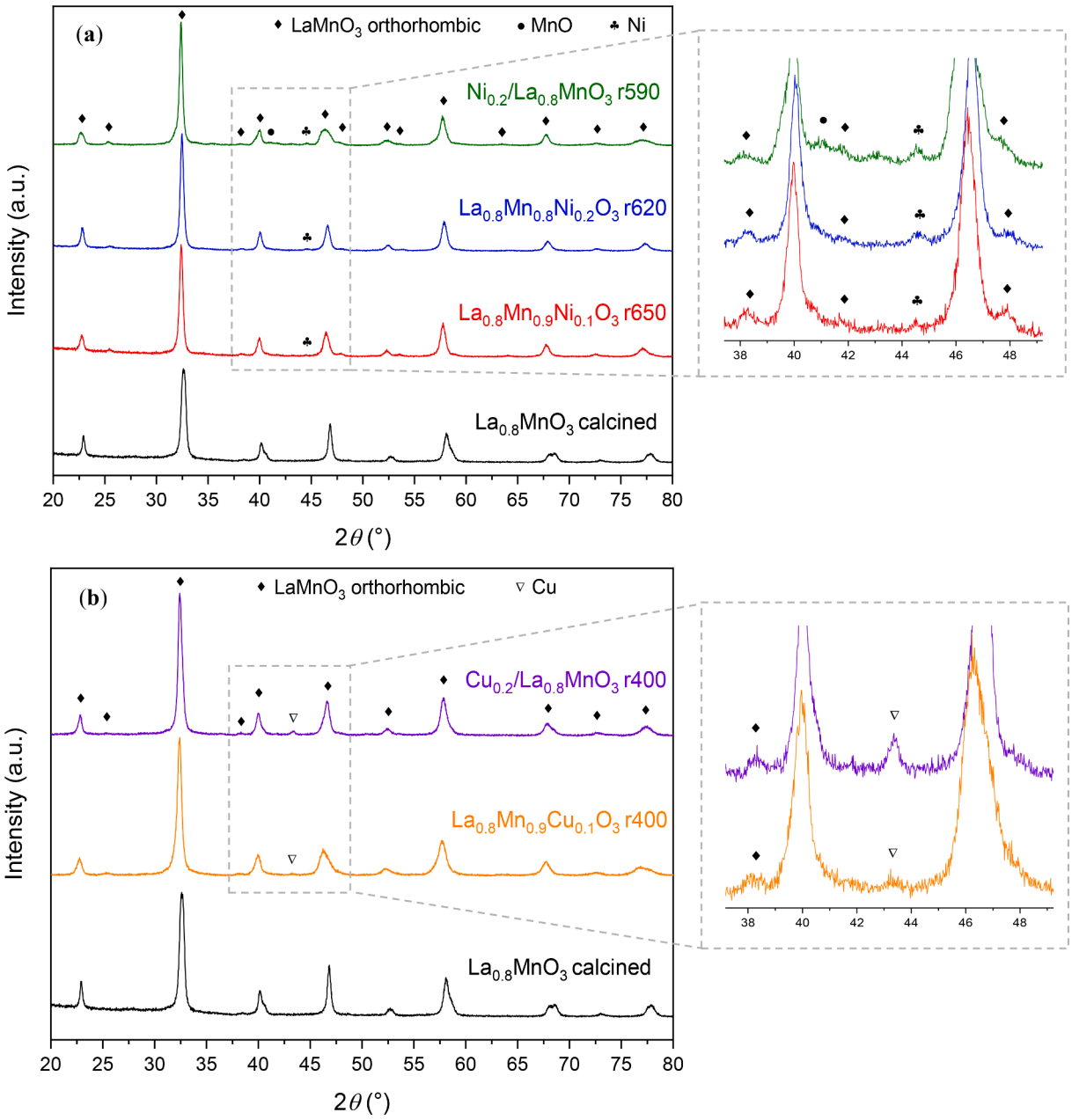

Fig. 2. XRD patterns of the reduced perovskites, compared to the reference calcined $La_{0.8}MnO_3$: (**a**) Ni-containing samples, with zoom on the region where Ni^0 reflections are spotted; (**b**) Cu-containing samples, with zoom on the region where Cu^0 reflections are spotted.

particles are formed, they easily dissociate H_2 molecules and the atomic H fragments can then be transferred to the perovskite support, accelerating its reduction [44,48]. Finally, the almost identical values of H_2 uptake for Ni-ADP and Cu-ADP samples, on both temperature regions, are once again in agreement with the hypothesis of a surface nanoparticles deposition without significant alteration of the underlying La-Mn oxide.

3.3. Elemental composition and surface features

In Table 4, semiquantitative analyses of the samples bulk and surface compositions are reported, respectively probed by EDX and XPS, on both calcined and reduced catalysts.

The bulk was often enriched in La at the expense of Mn, except for ADP samples where the La/Mn ratio was close to the nominal (stoichiometric) one; this holds true on both calcined and reduced samples. On the contrary, the surface of fresh samples was always enriched in Mn and depleted of La, possibly in the form of amorphous/dispersed MnO_x species as found elsewhere [40–42]; this could in principle by desirable to enhance the amount of catalytically active redox species at the surface. However, the reduction under diluted H_2 seemed to reverse this phenomenon, increasing the surface La/Mn ratio and, in the cases of B-site doping, pushing it to values even greater than 1. Regarding the loading of Ni and Cu, their amounts were generally very close to the expected one in the bulk (the only exception was some Cu defect on fresh $La_{0.8}Mn_{0.9}Cu_{0.1}O_3$), both on calcined and on reduced samples. It can be inferred that the performed reduction treatment, under 2 % H_2 for 2 h, did not substantially change the bulk chemical composition (higher reduction time might be necessary for this), as highlighted by both La/Mn and (Ni or Cu)/Mn ratios. Different behaviours emerged at the surface: Ni was always found in defective amount when doped at the B-site, likely confirming its incorporation inside the perovskite matrix

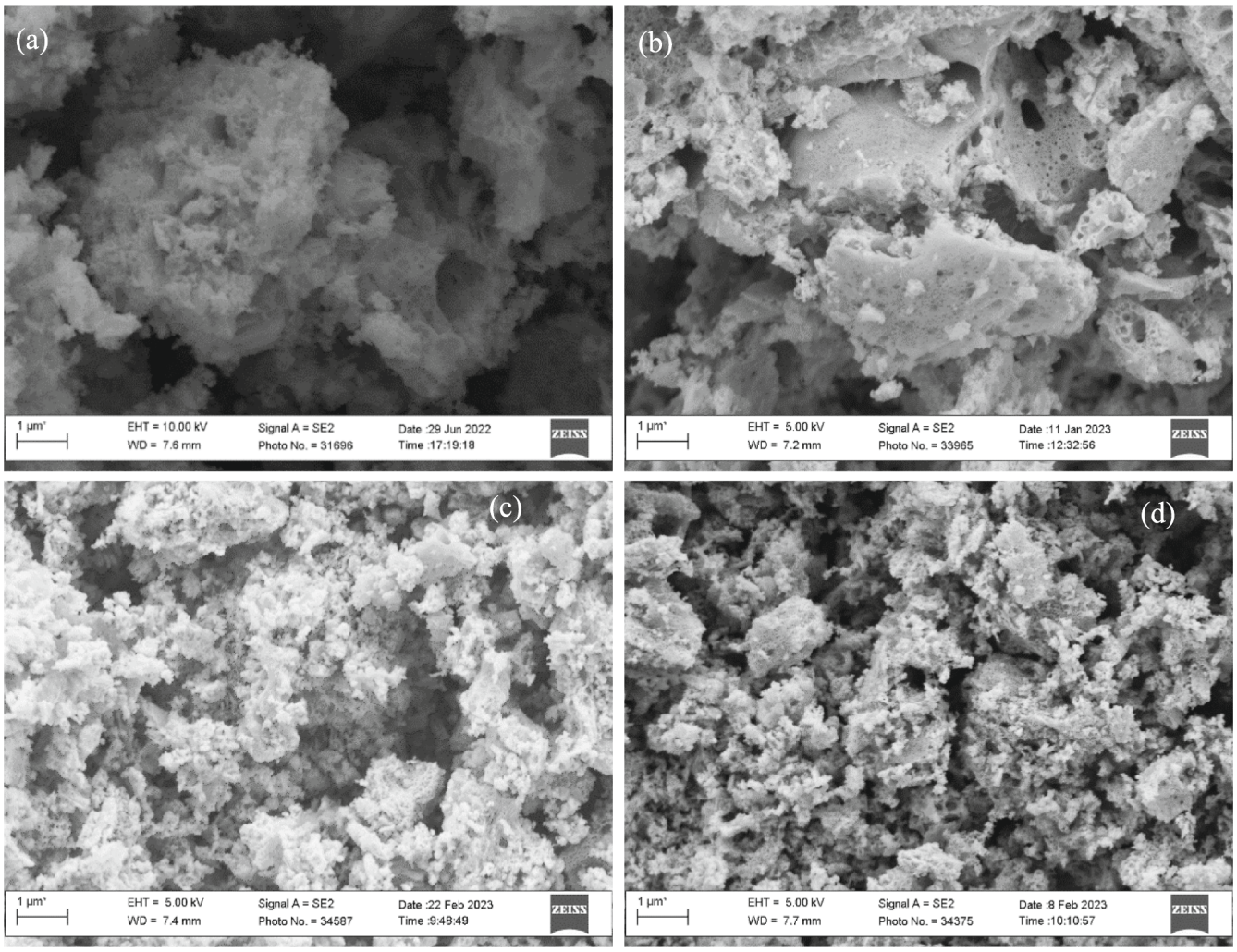

Fig. 3. SEM microhraphs at 25,000x magnification of (a) $La_{0.8}Mn_{0.9}Cu_{0.1}O_3$ fresh, (b) $La_{0.8}Mn_{0.9}Cu_{0.1}O_3$ r400, (c) $Ni_{0.2}/La_{0.8}MnO_3$ fresh, and (d) $Ni_{0.2}/La_{0.8}MnO_3$ r590.

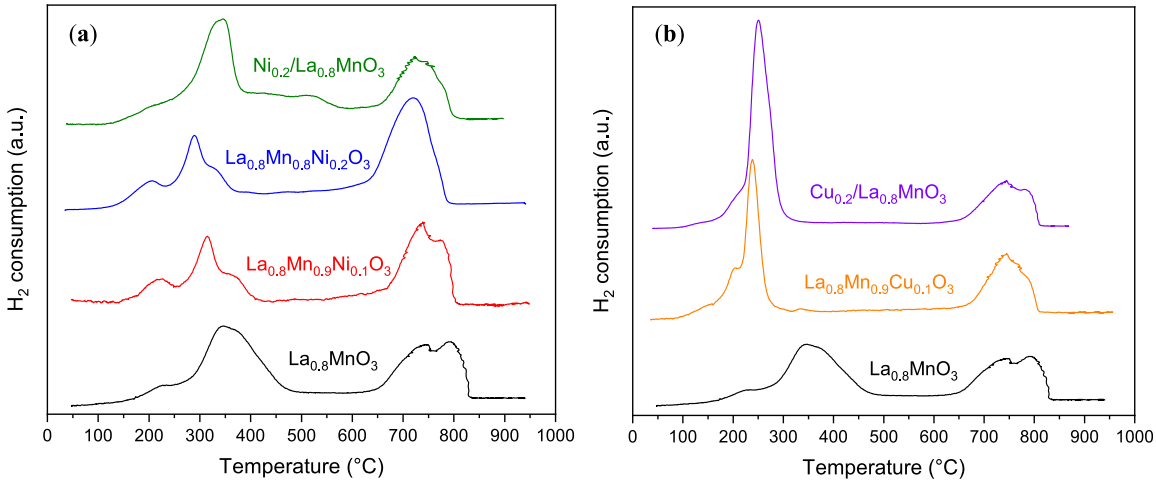

Fig. 4. H_2-TPR curves of: (**a**) Ni-containing samples, compared to the reference $La_{0.8}MnO_3$; (**b**) Cu-containing samples, compared to the reference $La_{0.8}MnO_3$.

(completely or mostly), even on sample $La_{0.8}Mn_{0.8}Ni_{0.2}O_3$ where an extra NiO phase was detected by XRD; on the contrary, Cu was found in excess at the surface of $La_{0.8}Mn_{0.9}Cu_{0.1}O_3$, suggesting a small incorporation inside the perovskite framework and a prevalent segregation as separated phases ($CuMn_2O_4$ + La_2CuO_4 as detected by XRD). The ADP procedure, instead, yielded an excess of both Ni and Cu XPS amounts, in agreement with a surface deposition onto the perovskite support. The reduction treatment did not significantly change the amount of surface

Table 3
Peak temperatures and quantitative analysis of H_2-TPR experiments.

Sample	Low temperature range			High temperature range		
	T_{max} (°C)	Experimental H_2 uptake (mol H_2/mol)	Theoretical* H_2 uptake (mol H_2/mol)	T_{max} (°C)	Experimental H_2 uptake (mol H_2/mol)	Theoretical H_2 uptake (mol H_2/mol)
$La_{0.8}MnO_3$	346	0.40	0.30[a]	794	0.28	0.50[b]
$La_{0.8}Mn_{0.9}Ni_{0.1}O_3$	315	0.29	0.35[a]	740	0.37	0.55[c]
$La_{0.8}Mn_{0.9}Cu_{0.1}O_3$	239	0.43	0.45[d]	745	0.31	0.45[b]
$La_{0.8}Mn_{0.8}Ni_{0.2}O_3$	298	0.26	0.40[a]	721	0.46	0.60[c]
$Ni_{0.2}/La_{0.8}MnO_3$	346	0.56	0.46[e]	724	0.26	0.44[b]
$Cu_{0.2}/La_{0.8}MnO_3$	251	0.57	0.46[d]	745	0.27	0.44[b]

* Calculated as if no oxygen excess/vacancies were present (oxygen stoichiometry = 3) and the charge imbalance was compensated by Mn^{4+} formation only.
[a] for the reduction step $Mn^{4+} \rightarrow Mn^{3+}$.
[b] for the reduction step $Mn^{3+} \rightarrow Mn^{2+}$.
[c] for the reduction steps $Mn^{3+} \rightarrow Mn^{2+}$ and $Ni^{2+} \rightarrow Ni^0$.
[d] for the reduction steps $Mn^{4+} \rightarrow Mn^{3+}$ and $Cu^{2+} \rightarrow Cu^+ \rightarrow Cu^0$.
[e] for the reduction steps $Mn^{4+} \rightarrow Mn^{3+}$ and $Ni^{2+} \rightarrow Ni^0$.

Table 4
Bulk (EDX) and surface (XPS) compositions of freshly calcined and reduced perovskites, surface chemical state.

Sample	La/Mn			(Ni or Cu)/Mn			$O_{OH,CO3}/O_L$	$C_{C=O}/C_{C-C}$
	EDX	XPS	nominal	EDX	XPS	nominal		
$La_{0.8}MnO_3$fresh	1.00	0.75	0.80	–	–	–	0.65	0.30
$La_{0.8}Mn_{0.9}Ni_{0.1}O_3$fresh	1.05	0.63	0.89	0.11	0.03	0.11	0.52	0.17
$La_{0.8}Mn_{0.9}Cu_{0.1}O_3$fresh	0.99	0.72	0.89	0.07	0.22	0.11	0.50	0.18
$La_{0.8}Mn_{0.8}Ni_{0.2}O_3$fresh	1.25	0.67	1.00	0.26	0.07	0.25	0.39	0.24
$Ni_{0.2}/La_{0.8}MnO_3$fresh	0.81	0.59	0.80	0.21	0.24	0.20	0.29	0.24
$Cu_{0.2}/La_{0.8}MnO_3$fresh	0.81	0.58	0.80	0.21	0.26	0.20	0.52	0.12
$La_{0.8}MnO_3$r400	0.97	0.84	0.80	–	–	–	0.67	0.32
$La_{0.8}MnO_3$r650	0.95	0.97	0.80	–	–	–	0.66	0.47
$La_{0.8}Mn_{0.9}Ni_{0.1}O_3$r650	1.01	1.17	0.89	0.10	0.06	0.11	0.77	0.27
$La_{0.8}Mn_{0.9}Cu_{0.1}O_3$r400	0.98	1.21	0.89	0.10	0.29	0.11	0.68	0.41
$La_{0.8}Mn_{0.8}Ni_{0.2}O_3$r620	1.08	1.16	0.80	0.25	0.08	0.25	0.62	0.80
$Ni_{0.2}/La_{0.8}MnO_3$r590	0.84	0.81	0.80	0.21	0.12	0.20	0.97	0.21
$Cu_{0.2}/La_{0.8}MnO_3$r400	0.81	0.69	0.80	0.21	0.28	0.20	0.41	0.53

Ni and Cu in many cases, although a certain enhancement was detected in $La_{0.8}Mn_{0.9}Ni_{0.1}O_3$ and $La_{0.8}Mn_{0.9}Cu_{0.1}O_3$ catalysts, which reasonably confirms that the exsolution of Ni^0/Cu^0 NPs occurred to a certain extent. A markedly different behaviour was observed for $Ni_{0.2}/La_{0.8}MnO_3$ ADP sample, in which the surface amount of Ni was halved in the reduced compared to the freshly calcined catalyst (yet in greater amount than on Ni B-site doped samples) suggesting the relevance of diffusion phenomena.

Detailed XPS spectra of O 1s and C 1s peaks are shown in Fig. 5 for representative samples. All the other XPS spectra (La 3d, Mn 2p, Cu 2p, Ni 3p) are reported in the Supporting Information, Figures S5-S9. O 1s spectra can be deconvoluted into three contributions: surface lattice oxygen (O_L) at about 529.5 eV, adsorbed OH^- and/or CO_3^{2-} species ($O_{OH,CO3}$) at 531 eV and residual adsorbed water (O_W) at 533 eV [35,62]. The dominant contribution was always O_L for all samples, but the ratio $O_{OH,CO3}/O_L$ (Table 4) tended to increase after reduction, with the only exception of $Cu_{0.2}/La_{0.8}MnO_3$. Similarly, C 1s peak can be well fitted by 3 components: C–C and C–H bonds at 284.8 eV, C-O bonds at 286 eV and C═O bonds at about 289 eV. All these contributions, including C-O and C═O bonds, are naturally present in surface carbon contamination, but a high percentage of the latter C═O subpeak can be ascribed to the presence of metal carbonates [63]: indeed, the ratio between the C═O and the C–C,C–H contributions (Table 4) tended to increase after reduction, for all samples except $Ni_{0.2}/La_{0.8}MnO_3$, in agreement with what was observed for $O_{OH,CO3}$. These observations, coupled to the increase of La/Mn ratio on reduced catalysts, suggest that the reductive treatment favoured the surface segregation of La(III) (oxy)hydroxides and (oxy)carbonates species. The reduction of metal oxides by H_2 and the consequent generation of H_2O is indeed expected to induce a surface hydroxylation, which is likely to occur to a greater extent for La^{3+} compared to Mn^{3+}, being the standard enthalpy of hydroxides formation ($\Delta_f H^\circ$) more negative for the former cation [64]; this would induce a preferential surface segregation of La rather than of Mn hydroxide in contact with H_2O. It is also known that La_2O_3 tends to rapidly form hydroxides, and carbonates to a lower extent, when exposed to ambient air [65], thus it is also possible that, once segregated on the surface, La^{3+} ions might be partially carbonated by CO_2 adsorption in ambient conditions. The interpretation of Mn $2p_{3/2}$ photopeak is complicated by the multiplet splitting effect which causes a peak broadening and asymmetric shape; in general, calcined $LaMnO_3$-related perovskites are known to possess a mixture of the +3 (predominant) and +4 oxidation states as indicated by the peak centre at ~ 642 eV [31,66,67], which is close to that of both pure Mn_2O_3 and MnO_2 oxides [68]; similar values were obtained for the samples prepared in this work as well (Fig. S6a, S7a, S8a). The reduction treatment did not shift the B.E. to significantly lower values (shifts of only 0.1–0.3 eV were observed), likely confirming that all Mn^{4+} cations were reduced to Mn^{3+} but not further to Mn^{2+} (pure MnO oxide is centred at ~ 641 eV), in agreement with the absence of a significant MnO phase on the XRD patterns of reduced samples. The position and shape of La $3d_{5/2}$ photopeak (Fig. S6b, S7b, S8b), i.e., ~ 834 eV with satellite at ~ 838 eV, is typical of the 3+ oxidation state, without significant variations before and after the reductive treatment [66]. Ni 2p photopeak is partially overlapped with the La 3d one, for this reason detailed spectra were also acquired at the Ni 3p level (Figure S9). The peak shape and position (67–67.5 eV), although poorly resolved in B-site doped compositions because of the low surface Ni amount, seems similar to that of pure NiO [69] on both calcined and reduced samples, suggesting the presence of Ni^{2+} cations even after the reductive

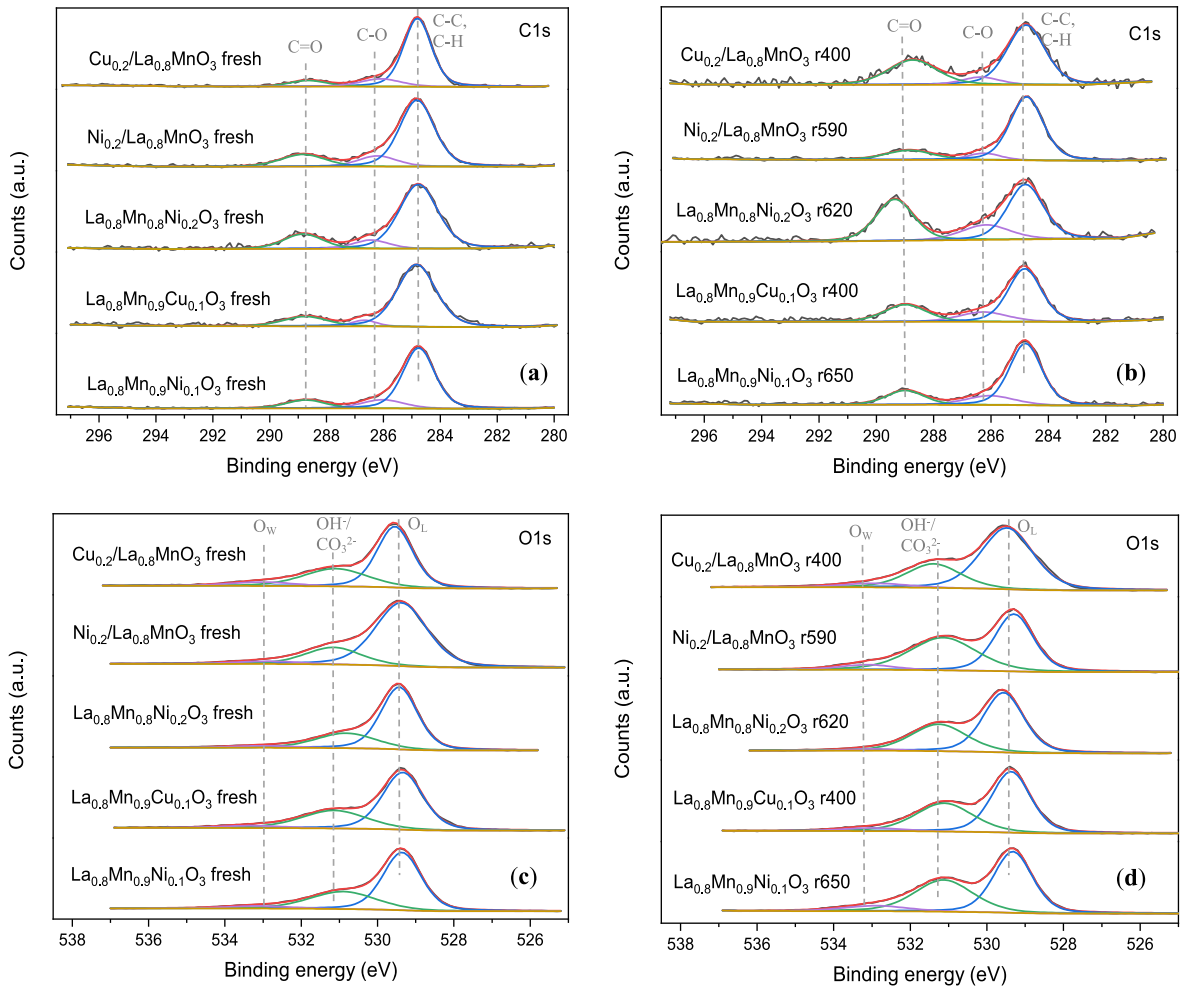

Fig. 5. Detailed XPS spectra and their deconvolution for Ni- and Cu-containing catalysts: (**a**) C 1s photopeak of fresh catalysts, (**b**) C 1s photopeak of reduced catalysts, (**c**) O 1s photopeak of fresh catalysts, (**d**) O 1s photopeak of reduced catalysts.

treatment; the reason for the absence of Ni^0 state (which was likely detected by XRD) probably lies in the fast surface reoxidation upon contact with the air atmosphere, before exposing the sample to UHV for XPS analysis. A similar consideration can be formulated for the Cu 2p photopeak (Fig. S7c): the binding energy value of 933.5–933.7 eV and the presence of satellites in the range 938–948 eV, for both calcined and reduced catalysts, are typical features of the Cu^{2+} oxidation state [20]; again, a fast surface reoxidation of Cu^0 NPs (detected by XRD) seemed to occur in contact with ambient air.

Representative reduced samples were further characterized by HAADF STEM imaging coupled with EDX elemental mapping. The results are reported in Figure S10 for La, Mn and O, and in Fig. 6 for Ni and Cu elements. EDX maps were necessary to clearly observe the metallic nanoparticles (NPs) of Ni and Cu, which could not be distinguished from the perovskite matrix on morphological images alone; the corresponding NPs size distribution estimated from the EDX maps is also shown in Fig. 6. The features of metallic NPs were different, depending both on the kind of metal as well as on the procedure for metal loading on perovskite, among ADP and B-site doping followed by reduction/exsolution. Cu NPs obtained from $La_{0.8}Mn_{0.9}Cu_{0.1}O_3$ reduction (Fig. 6b) were the smallest, 13 nm on average, suggesting that exsolution and/or decomposition of mixed La-Cu and Mn-Cu phases produced relatively well dispersed NPs featuring a good metal-support interaction, although they were not uniformly distributed in the whole probed area and in some other regions (not shown) they were not even observed. Ni NPs on $La_{0.8}Mn_{0.8}Ni_{0.2}O_3$ (Fig. 6a) had a broader size distribution, with average size of around 20 nm, likely because they resulted partially from exsolution and partially from reduction of segregated NiO particles. In both cases, the exsolution of Cu or Ni from the perovskite matrix was not complete, given the presence of atomically dispersed Cu or Ni species throghout the whole samples, ascribed to residual Ni^{2+} and Cu^{2+} cations stabilized in the perovskite lattice.

The Ni NPs deposited by ADP on $Ni_{0.2}/La_{0.8}MnO_3$ sample (Fig. 6c) were charcaterized by a much higher density compared to NPs on the B-site doped sample, also in line with the higher Ni XPS concentration on the former, while the size distribution was only slightly bigger (on average 22 nm) than on the $La_{0.8}Mn_{0.8}Ni_{0.2}O_3$ sample, despite some tendency to agglomerate was spotted. Cu NPs on $Cu_{0.2}/La_{0.8}MnO_3$ (Fig. 6d) had a very broad size distribution and were affected by a strong tendency to agglomerate, producing aggregates of up to 70–80 nm of size, despite the average size (~26 nm) was not much higher than on $Ni_{0.2}/La_{0.8}MnO_3$. The strong agglomeration also suggests a weak metal-support interaction. The higher tendency of Cu to diffuse and produce agglomerates of NPs with respect to Ni was similarly observed by us on a $La_{0.9}FeO_3$ support [70].

3.4. Catalytic activity

The prepared calcined and pre-reduced catalysts were tested in the combustion of CH_4 to CO_2 under a stoichiometric amount of O_2, as a model reaction occurring on methane-fed vehicles Three-Way catalytic converters (TWC) [7]. CH_4 light-off conversion curves are reported in

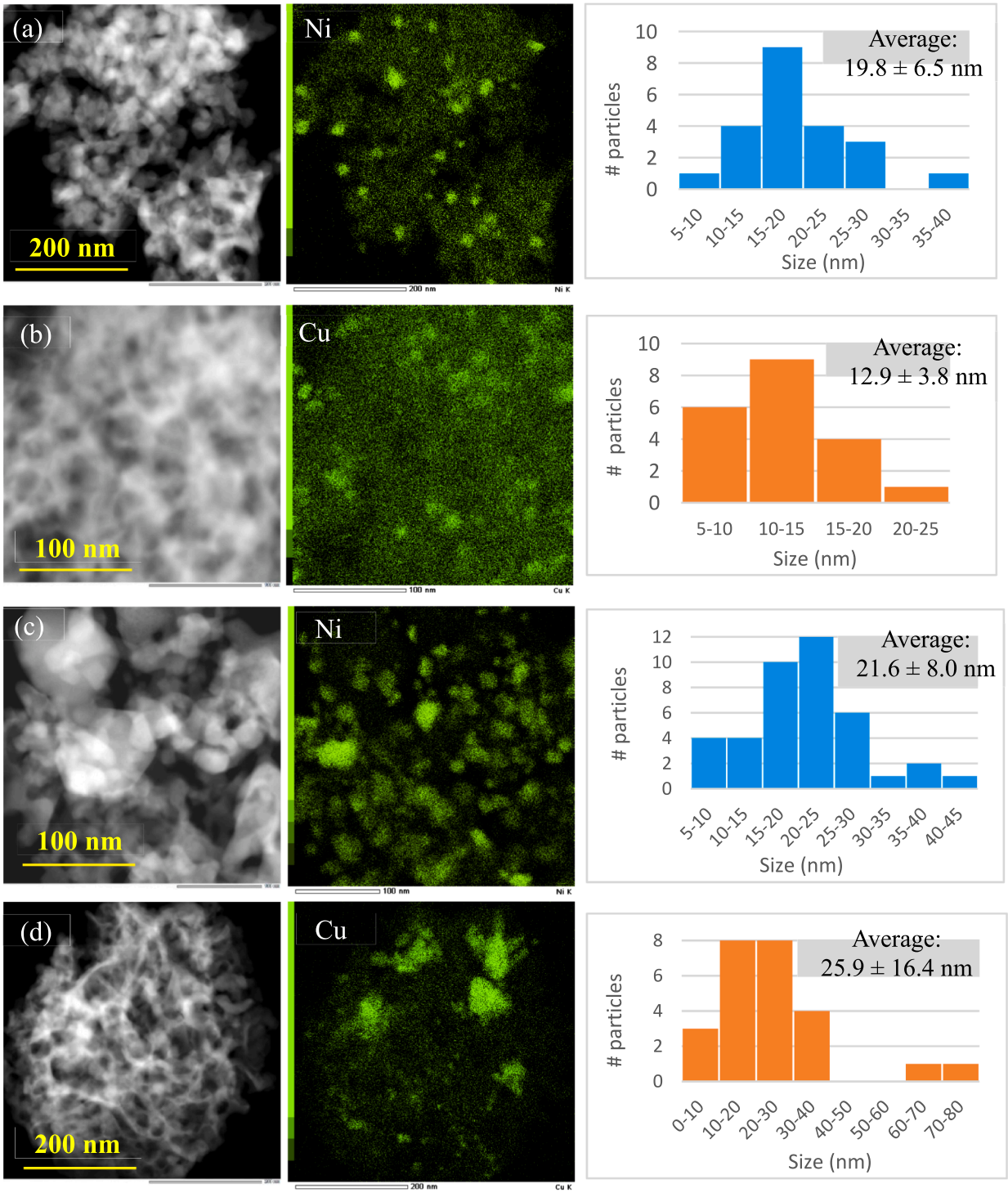

Fig. 6. HAADF-STEM morphological images and corresponding EDX mapping of Ni or Cu in reduced samples: (a) $La_{0.8}Mn_{0.8}Ni_{0.2}O_3$ r620, (b) $La_{0.8}Mn_{0.9}Cu_{0.1}O_3$ r400, (c) $Ni_{0.2}/La_{0.8}MnO_3$ r590 and (d) $Cu_{0.2}/La_{0.8}MnO_3$ r400. Inset: nanoparticles size distribution measured from EDX maps.

Fig. 7, while the values of T_x (temperature necessary to achieve x% CH_4 conversion, with x = 10, 50, 90) and the reaction rates at 500 °C are listed in Table 5.

For comparison, Ponce et al. studied CH_4 combustion with stoichiometric O_2 on $La_{1-x}Sr_xMnO_3$ perovskites, achieving T_{50} values greater than 550 °C and T_{90} values slightly above 700 °C [35]; Zaza et al. tested $La_{1-x}Sr_xFeO_3$ compositions, still in stoichiometric CH_4/O_2 mixture, reaching a T_{50} slightly below 550 °C for x = 0.2, but did not reach 90 % conversion even at 800 °C [71]. Hence, looking at the T_{50} and T_{90} values reported in Table 5, it is evident that several of the catalysts prepared in the present work showed a comparable or improved performance with respect to the previous works.

All the prepared catalysts produced CO_2 with selectivity close to 100 % as product of CH_4 oxidation (very low and hardly quantifiable amounts of CO were detected in some cases, probably in the range of tens of ppm), since the stoichiometric amount of O_2 in the gaseous mixture and the ability of LaMn-perovskites to release active oxygen in general prevent uncomplete combustion. The perovskite synthesis

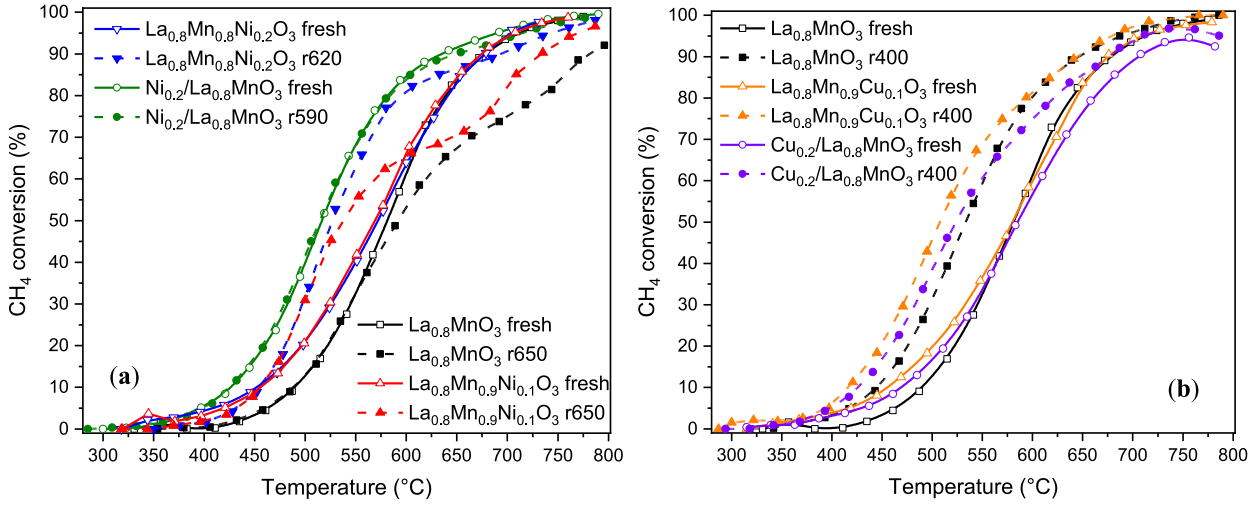

Fig. 7. CH_4 light-off conversion curves of the freshly calcined and reduced perovskites: (**a**) Ni-containing samples, referenced to $La_{0.8}MnO_3$ support; (**b**) Cu-containing samples, referenced to $La_{0.8}MnO_3$ support. Freshly calcined catalysts are plotted with full lines and open symbols, reduced catalysts with dashed lines and full symbols.

Table 5
CH_4 oxidation performance of the prepared catalysts: temperature of 10 %, 50 % and 90 % CH_4 conversion, specific and intrinsic reaction rates at 500 °C.

Sample	T_{10} (°C)	T_{50} (°C)	T_{90} (°C)	$r_{specific}$ (mol/s/g)	$r_{intrinsic}$ (mol/s/m^2)
$La_{0.8}MnO_3$ fresh	489	581	678	3.2×10^{-6}	1.3×10^{-7}
$La_{0.8}Mn_{0.9}Ni_{0.1}O_3$ fresh	455	569	675	5.1×10^{-6}	1.2×10^{-7}
$La_{0.8}Mn_{0.9}Cu_{0.1}O_3$ fresh	455	580	676	4.8×10^{-6}	1.3×10^{-7}
$La_{0.8}Mn_{0.8}Ni_{0.2}O_3$ fresh	452	572	678	5.0×10^{-6}	1.3×10^{-7}
$Ni_{0.2}/La_{0.8}MnO_3$ fresh	426	517	635	8.2×10^{-6}	2.9×10^{-7}
$Cu_{0.2}/La_{0.8}MnO_3$ fresh	469	585	706	4.1×10^{-6}	1.8×10^{-7}
$La_{0.8}MnO_3$ r400	444	533	646	6.9×10^{-6}	2.8×10^{-7}
$La_{0.8}MnO_3$ r650	488	592	781	3.2×10^{-6}	1.3×10^{-7}
$La_{0.8}Mn_{0.9}Ni_{0.1}O_3$ r650	455	538	733	7.0×10^{-6}	1.6×10^{-7}
$La_{0.8}Mn_{0.9}Cu_{0.1}O_3$ r400	416	508	645	9.0×10^{-6}	2.4×10^{-7}
$La_{0.8}Mn_{0.8}Ni_{0.2}O_3$ r620	454	527	694	7.0×10^{-6}	1.9×10^{-7}
$Ni_{0.2}/La_{0.8}MnO_3$ r590	425	515	650	8.5×10^{-6}	3.0×10^{-7}
$Cu_{0.2}/La_{0.8}MnO_3$ r400	426	524	676	8.1×10^{-6}	3.4×10^{-7}

protocol by citrate combustion was previously optimized to achieve the highest possible surface area, Mn^{4+} reducibility and surface as well as bulk oxygen mobility, crucial factors for enhancing CH_4 activation. A further improvement at temperatures below 600 °C were obtained on the fresh B-site doped samples (T_{10} = 452–455 °C) compared to calcined $La_{0.8}MnO_3$ (T_{10} = 489 °C) [58]. The higher surface area arising from B-site doping accelerated the release of surface oxygen species, thus promoting the suprafacial mechanism occurring at low temperatures, whereas the intrafacial mechanism, likely triggered above 600 °C [37], were not affected by doping. There were no marked differences among Ni and Cu dopants, nor among different Ni contents at B-site (10 mol% or 20 mol%), suggesting that the same type of active site is involved for all compositions and the only discriminant factor is the higher SSA (thus greater number of active sites) provided by doping. An analogous consideration can be deduced by the values of intrinsic reaction rates (normalized by BET surface areas) at 500 °C, which were identical for all B-site doped samples as well as for $La_{0.8}MnO_3$. Remarkably, $Ni_{0.2}/La_{0.8}MnO_3$ nanocomposite showed superior performance compared to all other compositions in the calcined state, achieving 90 % conversion already at 635 °C (T_{90} > 670 °C for the other catalysts). In parallel, this sample showed higher values of both specific and intrinsic rates, evidencing that a different kind of active site is involved, which is assumed to be the interface between NiO NPs and perovskite support. For comparison, a Ni/ZrO_2 catalyst was analogously prepared by ADP, as detailed in the SI, and tested for CH_4 conversion as reported in Figure S11. NiO particles loaded on inert ZrO_2 support performed much worse than $Ni_{0.2}/La_{0.8}MnO_3$ (and even worse than the benchmark $La_{0.8}MnO_3$), only reaching 70 % conversion at 800 °C; this would confirm that the presence of a reducible support like $LaMnO_3$ is crucial, being able to provide active oxygen species at the NiO interface to assist CH_4 activation. A similar metal-support synergistic effect was reported comparing NiO/CeO_2 and NiO/SiO_2 catalysts, the former being more active in CH_4 oxidation thanks to the oxygen exchange capability of the support [54]. Instead, the loading of CuO NPs by ADP was not favourable to increase CH_4 oxidation performances: only a modest increase in activity at T < 550 °C was observed for $Cu_{0.2}/La_{0.8}MnO_3$ compared to bare $La_{0.8}MnO_3$, but the perovskite alone became more active above 575 °C. Thus, NiO is clearly more active than CuO for CH_4 combustion, as also revealed by the lower intrinsic rate observed on the Cu-ADP sample with respect to the Ni-ADP one. Similar results were obtained by Liu et al. [12].

It is interesting to note that the $La_{0.8}MnO_3$ perovskite itself displayed very different catalytic activity depending on the temperature of pre-reduction: a marked improvement of CH_4 conversion was achieved by pre-treatment at 400 °C (T_{50} = 533 °C with respect to 581 °C of the fresh sample), whereas a decrease in the high temperature activity occurred upon reduction at 650 °C (T_{90} = 781 °C compared to 678 °C of the calcined counterpart). The reason for the former observation could be that the partial Mn^{4+} to Mn^{3+} reduction, occurring at 400 °C according to H_2-TPR, generated more oxygen vacancies (V_O) which would favour the reactant adsorption and/or the mobility of active oxygen species. On the contrary, the reduction at 650 °C leaved no residual Mn^{4+} cations in the perovskite lattice, and the subsequent Mn^{3+} reoxidation under reaction conditions depleted some O_2 from the inlet stream, worsening CH_4 conversion and producing a two-steps conversion curve. This is confirmed by the XRD pattern of spent $La_{0.8}MnO_3$ r650 catalyst (Figure S3), in which the rhombohedral structure characteristic of the calcined powder was recovered, indicative of the mixed Mn^{3+}/Mn^{4+} state. It is also suggested that a certain amount of Mn^{4+} ions in the

perovskite structure are crucial to ensure a good oxidation activity.

The reduced Ni-doped catalysts, $La_{0.8}Mn_{0.9}Ni_{0.1}O_3$ and especially $La_{0.8}Mn_{0.8}Ni_{0.2}O_3$, displayed some improvement of CH_4 conversion, at intermediate temperatures only (from 450 to 600/650 °C), reasonably due to the exsolution of a certain number of active Ni NPs: for instance, the T_{50} was decreased from 572 °C of the fresh $La_{0.8}Mn_{0.8}Ni_{0.2}O_3$ to 527 °C after reduction. However, the issue of perovskite reoxidation at high temperatures (above ~ 650 °C) that worsened CH_4 conversion was still observed, in particular for $La_{0.8}Mn_{0.9}Ni_{0.1}O_3$. A high reduction temperature (> 600 °C) is thus quite detrimental in this sense, which however is in contrast with the requirements for Ni exsolution, already limited according to surface Ni concentrations by XPS. Concerning the Ni-ADP catalyst, its performance was nearly unchanged after the reductive treatment, with only a marginal decrease above 600 °C because of the perovskite reoxidation issue, yet retaining higher activity than the B-site doped samples. It is suggested that the mechanism of CH_4 oxidation on Ni sites could involve cycles of reduction–oxidation of the Ni^{2+}/Ni^0 redox couple [54], thus producing an identical activity irrespective of the initial presence of NiO or Ni^0 NPs; in addition, partial coverage by chemisorbed O_2 might occur on Ni^0 surface, in line with XPS Ni 3p spectra. The dominant factor for improving catalytic activity in Ni-$LaMnO_3$ nanocomposites seems therefore the number of Ni active sites, which were higher on Ni-ADP sample compared to B-site doped ones, even after reduction/exsolution, as revealed by both XPS and STEM-EDX.

Both Cu-containing catalysts, $La_{0.8}Mn_{0.9}Cu_{0.1}O_3$ and $Cu_{0.2}/La_{0.8}MnO_3$, achieved markedly better CH_4 conversion after the reductive treatment at 400 °C, with T_{50} lowered to 508 and 524 °C, respectively, compared to 580 and 585 °C for the fresh samples. Below 550/600 °C, their performances were also higher compared to the reference $La_{0.8}MnO_3$ r400 catalyst (T_{50} = 533 °C), indicating that the enhancement is not only due to the partial $Mn^{4+} \rightarrow Mn^{3+}$ reduction of perovskite, but also to the higher activity of reduced Cu species, either Cu^0 or Cu^+, compared to Cu^{2+}. A similar conclusion was provided by Esmaeilnejad-Ahranjani et al., who observed a transient increase in propane combustion performance when reducing Cu^{2+}, which was attributed mainly to active Cu^+ species [44]. The subsequent reoxidation to Cu^{2+} inside the reaction mixture (likely occurring at ~ 600 °C) suppresses this improved performance compared to the bare perovskite. Among the two Cu-containing catalysts, the B-site doped one was more active than the ADP one in the whole temperature range, the latter showing some performance degradation at temperatures > 750 °C, which in fact was detected even on the fresh counterpart. This is most likely the effect of the smaller NPs size and good metal-support interaction characterizing the $La_{0.8}Mn_{0.9}Cu_{0.1}O_3$ r400 sample, as opposed to the strong NPs agglomeration on $Cu_{0.2}/La_{0.8}MnO_3$ r400, as observed by STEM-EDX micrographs.

Among all the prepared catalysts, the Cu-doped one was the best performing after pre-reduction, even slightly better than $Ni_{0.2}/La_{0.8}MnO_3$.

The long-term stability of the two best performing catalysts, i.e. fresh $Ni_{0.2}/La_{0.8}MnO_3$ and pre-reduced $La_{0.8}Mn_{0.9}Cu_{0.1}O_3$, was investigated through a 18 h-long test at 600 °C in the same reaction mixture as for light-off experiments. For comparison, the same durability test was carried on fresh $La_{0.8}MnO_3$ perovskite. The results are reported in Fig. 8. Let us note that, for all catalysts, the conversion of CH_4 during the ramping up stage of the stability tests was very similar to the values obtained throughout light-off tests, with deviations not larger than 2.5 % at 600 °C, highlighting a good data reproducibility. In detail, $La_{0.8}MnO_3$ reached a maximum CH_4 conversion of 63 % and showed only a marginal loss of 3.5 % over the 18 h-period, likely due to a modest thermal sintering. Ni-ADP and Cu-exsolved catalysts performed better, with maximum conversion at 600 °C of respectively 83 % and 79 %, similarly to light-off tests, but were characterized by a faster performance loss over the first 2–3 h on stream. The Ni-perovskite nanocomposite had the fastest degradation, going below the performance of $La_{0.8}Mn_{0.9}Cu_{0.1}O_3$ after the first hour at 600 °C and keeping a residual CH_4 conversion of nearly 70 % after 18 h. The Cu-doped catalyst was more stable after the first few hours, retaining 72 % conversion at the end of the timeframe. The more prominent loss of activity affecting $Ni_{0.2}/La_{0.8}MnO_3$ could be caused by the weaker metal-support interaction characterizing NPs loaded by ADP, producing more agglomerates which would decrease the number of active Ni-perovskite interface sites. The NPs obtained by exsolution or mixed oxides decomposition on $La_{0.8}Mn_{0.9}Cu_{0.1}O_3$ were probably more resistant to thermal sintering and the initial performance loss might result mainly from the reoxidation of active Cu^0/Cu^+ species (as well as of Mn^{3+} to Mn^{4+}).

The spent catalysts were characterized from the structural point of view by XRD. Their diffraction patterns are reported in Figure S12 and S13 concerning powders subjected to light-off experiments up to 800 °C (after the pre-reductive treatment in 2 % H_2/Ar), and in Figure S14 for the catalysts subjected to durability tests at 600 °C. The original

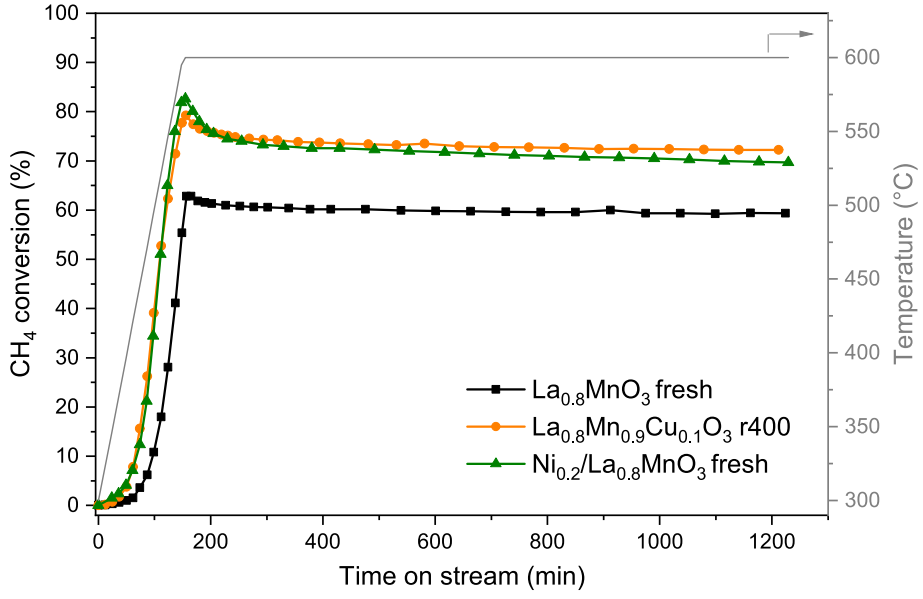

Fig. 8. CH_4 conversion during stability tests at 600 °C for 18 h on stream.

rhombohedral $LaMnO_3$ perovskite structure was restored for all catalysts in a globally oxidizing reaction mixture, highlighting a good structural reversibility; the reflection splitting characteristic of the rhombohedral symmetry was often more evident on spent catalysts at 800 °C compared to freshly calcined samples, but not for powders recovered from the long-term test at 600 °C. Thus, a more prominent growth of perovskite grains due to thermal sintering occurred when reaching high temperatures (above the calcination T of 750 °C), even for a short time, rather than when stationing for long times at lower temperatures. Some minor phases often appeared or became more pronounced on spent catalysts after reaching 800 °C. Mn_3O_4 impurities were detected for spent $La_{0.8}MnO_3$, $La_{0.8}Mn_{0.9}Ni_{0.1}O_3$ and $La_{0.8}Mn_{0.9}Cu_{0.1}O_3$, coupled with a more evident La_2CuO_4 phase on the latter; hence, the perovskite structure might have become less A-site deficient and/or amorphous MnO_x species originally present on the sample surface might have formed larger and less dispersed crystallites. On the contrary, $La_{0.8}Mn_{0.9}Cu_{0.1}O_3$ after the 18 h test at 600 °C only showed the appearance of La_2CuO_4 and $CuMn_2O_4$ phases, as on the calcined powder, confirming that reoxidation is the most probable reason for the activity loss on the pre-reduced catalyst. Regarding $La_{0.8}Mn_{0.8}Ni_{0.2}O_3$, weak impurities of NiO and of $NiMn_2O_4$ spinel were detected on the spent sample after light-off test at 800 °C, as well as on the fresh one, but the spinel phase become slightly more evident after reaction. An even more pronounced crystallization of a side spinel phase ($NiMn_2O_4$ or $CuMn_2O_4$) was found on both ADP samples after reaching 800 °C, which was not detected on the fresh samples; this suggests a less A-site deficient perovskite support was formed as well, along with the formation of Mn-Ni or Mn-Cu solid solutions from originally deposited NiO_x or CuO_x particles. The Ni-ADP catalyst after durability test at 600 °C showed the growth of the spinel phase as well, but to a much lower extent than after test at 800 °C. This would likely confirm the main cause of deactivation in the long-term test to be NPs sintering and loss of Ni-perovskite interface.

4. Conclusions

In the present work, A-site deficient La_xMnO_3 perovskites, functionalized with non-noble metals Ni and Cu, were studied as potential catalysts for CH_4 combustion in stoichiometric conditions, as cheaper alternative to traditional Pd-based ones. This reaction is of interest for the abatement of unburned CH_4 residues on methane-fed engines. Two different metal loading protocols were investigated: i) B-site perovskite doping with Ni^{2+} or Cu^{2+} cations; ii) Ammonia-driven Deposition-Precipitation (ADP), to deposit NiO or CuO nanoparticles onto the perovskite surface. An improvement of perovskite morphology (surface area, porosity) and of Mn^{4+} reducibility was observed on all B-site doped compositions, while CuO and NiO deposition did not significantly modify the support textural features. Subsequently, a reductive treatment under diluted H_2 promoted reduction to Ni^0 and Cu^0 nanoparticles (NPs) and a partial exsolution in the case of B-site doping. The amount of Ni at surface was low for doped compositions, high for the ADP sample, whereas Cu was always present at high surface concentrations. Catalytic activity of fresh (calcined) catalysts was slightly improved at low temperatures after B-site doping with either metal, thanks to more favourable surface area and reducibility of the perovskite itself. NiO-ADP showed a remarkable catalytic activity, ascribed to a cooperative effect of the metal oxide-perovskite support interface, while CuO-ADP did not bring such favourable performances. After reduction and partial exsolution, Ni-doped perovskites could increase the catalytic activity in a limited extent because of a rather low Ni surface concentration and NPs density, whereas a good performance was retained for Ni-ADP catalyst thanks to the higher concentration of this metal at the surface and the higher NPs density. Reduced Cu species (likely Cu^+) were shown to improve catalytic activity compared to oxidized Cu^{2+}, and the effect was more pronounced on the Cu-doped sample because of lower NPs size and stronger metal-support interaction compared to Cu-ADP catalyst, the latter showing a strong NPs agglomeration and some signs of deactivation at high temperatures. Hence, the most promising catalysts among those investigated in this work were $Ni_{0.2}/La_{0.8}MnO_3$ prepared by ADP and $La_{0.8}Mn_{0.9}Cu_{0.1}O_3$ with doping at B-site, the latter showing a better long-term stability because of more favourable metal-support interaction achieved by exsolution, limiting NPs sintering. Future work will be focused on the variation of the inlet CH_4/O_2 ratio around the stoichiometric point, to mimic the oscillating reducing/oxidizing conditions typical of TWC systems, as well as on the investigation of H_2O-containing mixtures, a potential inhibitor always present in real engine exhausts.

CRediT authorship contribution statement

Andrea Osti: Writing – original draft, Visualization, Validation, Project administration, Formal analysis, Conceptualization. **Lorenzo Rizzato:** Writing – review & editing, Visualization, Validation, Investigation. **Simone Costa:** Writing – review & editing, Validation, Investigation. **Jonathan Cavazzani:** Writing – review & editing, Visualization, Validation, Investigation. **Antonella Glisenti:** Writing – review & editing, Supervision, Resources, Project administration, Methodology, Funding acquisition.

Declaration of competing interest

The authors declare that they have no known competing financial interests or personal relationships that could have appeared to influence the work reported in this paper.

Data availability

Data will be made available on request.

Acknowledgements

This work was financially supported by the European Union HORIZON EUROPE Programme under grant agreement number 101091534 KNOWSKITE-X.

The authors thank “Sviluppo delle infrastrutture e programma degli interventi del Consiglio Nazionale delle Ricerche (2019)” for funding the XPS spectrometer.

A special thank goes to dr. Andrea Basagni (University of Padova) for the STEM-EDX analysis, and to prof. Marco Scavini (University of Milan) for providing high-resolution XRD measurements at the ID22 beamline, ESRF synchrotron, Grenoble.

Appendix A. Supplementary data

Supplementary data to this article can be found online at https://doi.org/10.1016/j.fuel.2024.133368.

References

[1] IEA. Outlook for biogas and Prospects for organic growth. World Energy Outlook, Special Report biomethane; 2020.
[2] Jung S, Lee J, Moon DH, Kim KH, Kwon EE. Upgrading biogas into syngas through dry reforming. Renew Sust Energ Rev 2021;143:110949. https://doi.org/10.1016/j.rser.2021.110949.
[3] Minh NQ, Takahashi T. Electrode reaction. In: Minh NQ, Takahashi T, editors. Science and Technology of Ceramics Fuel Cells, Elsevier Science Ltd; 1995, p. 199-232. Doi: 10.1016/B978-0-444-89568-4.X5001-4.
[4] Raj A. Methane emission control. Johnson Matthey Technol Rev 2016;60:228–35. https://doi.org/10.1595/205651316X692554.
[5] Boucher O, Friedlingstein P, Collins B, Shine KP. The indirect global warming potential and global temperature change potential due to methane oxidation. Environ Res Lett 2009;4:044007. https://doi.org/10.1088/1748-9326/4/4/044007.
[6] Yang J, Guo Y. Nanostructured perovskite oxides as promising substitutes of noble metals catalysts for catalytic combustion of methane. Chinese Chem Lett 2018;29:252–60. https://doi.org/10.1016/j.cclet.2017.09.013.

[7] Huang C, Shan W, Lian Z, Zhang Y, He H. Recent advances in three-way catalysts of natural gas vehicles. Catal Sci Technol 2020;10:6407–19. https://doi.org/10.1039/d0cy01320j.

[8] Yoshida H, Hirakawa T, Oyama H, Nakashima R, Hinokuma S, Machida M. Effect of thermal aging on local structure and three-way catalysis of Cu/Al2O3. J Phys Chem C 2019;123:10469–76. https://doi.org/10.1021/acs.jpcc.9b01848.

[9] Feng Y, Rao PM, Kim DR, Zheng X. Methane oxidation over catalytic copper oxides nanowires. P Combust Inst 2011;33:3169–75. https://doi.org/10.1016/j.proci.2010.05.017.

[10] Yang W, Li D, Xu D, Wang X. Effect of CeO2 preparation method and Cu loading on CuO/CeO2 catalysts for methane combustion. J Nat Gas Chem 2009;18:458–66. https://doi.org/10.1016/S1003-9953(08)60141-3.

[11] Huang L, Zhang X, Chen L, Lei L. Promotional effect of CeO2 and Y2O3 on CuO/ZrO2 catalysts for methane combustion. J Rare Earths 2012;30:123–7. https://doi.org/10.1016/S1002-0721(12)60007-6.

[12] Liu F, Sang Y, Ma H, Li Z, Gao Z. Nickel oxide as an effective catalyst for catalytic combustion of methane. J Nat Gas Sci Eng 2017;41:1–6. https://doi.org/10.1016/j.jngse.2017.02.025.

[13] Huang X, Li J, Wang J, Li Z, Xu J. Catalytic combustion of methane over a highly active and stable NiO/CeO2 catalyst. Front Chem Sci Eng 2020;14:534–45. https://doi.org/10.1007/s11705-019-1821-4.

[14] Zhang X, House SD, Tang Y, Nguyen L, Li Y, Opalade AA, et al. Complete oxidation of methane on NiO nanoclusters supported on CeO2 nanorods through synergistic effect. ACS Sustain Chem Eng 2018;6:6467–77. https://doi.org/10.1021/acssuschemeng.8b00234.

[15] Chen J, Carlson BD, Toops TJ, Li Z, Lance MJ, Karakalos SG, et al. Methane combustion over Ni/CexZr1–xO2 catalysts: impact of ceria/zirconia ratio. ChemCatChem 2020;12:5558–68. https://doi.org/10.1002/cctc.202000947.

[16] Zhang S, Lee J, Kim DH, Kim T. Effects of Ni loading on the physicochemical properties of NiO: X/CeO2 catalysts and catalytic activity for NO reduction by CO. Catal Sci Technol 2020;10:2359–68. https://doi.org/10.1039/c9cy02619c.

[17] Peña MA, Fierro JLG. Chemical structures and performance of perovskite oxides. Chem Rev 2001;101:1981–2017. https://doi.org/10.1021/cr980129f.

[18] Zhu X, Li K, Neal L, Li F. Perovskites as geo-inspired oxygen storage materials for chemical looping and three-way catalysis: a perspective. ACS Catal 2018;8:8213–36. https://doi.org/10.1021/acscatal.8b01973.

[19] Pinto D, Glisenti A. Pulsed reactivity on LaCoO3-based perovskites: a comprehensive approach to elucidate the CO oxidation mechanism and the effect of dopants. Catal Sci Technol 2019;9:2749–57. https://doi.org/10.1039/c9cy00210c.

[20] Wu J, Dacquin JP, Djelal N, Cordier C, Dujardin C, Granger P. Calcium and copper substitution in stoichiometric and La-deficient LaFeO3 compositions: a starting point in next generation of Three-Way-Catalysts for gasoline engines. Appl Catal B Environ 2021;282:119621. https://doi.org/10.1016/j.apcatb.2020.119621.

[21] Wu J, Zheng Y, Dacquin JP, Djelal N, Cordier C, Dujardin C, et al. Impact of dual calcium and manganese substitution of La-deficient perovskites on structural and related catalytic properties: future opportunities in next three-way-catalyst generation? Appl Catal A Gen 2021;619:118137. https://doi.org/10.1016/j.apcata.2021.118137.

[22] Brusamarello E, Blonda C, Salazar-Castro C, Pascui AE, Canu P, Glisenti A. Industrially produced Fe- And Mn-based perovskites: effect of synthesis on reactivity in three-way catalysis: Part 1. ACS Omega 2021;6:24325–37. https://doi.org/10.1021/acsomega.1c02133.

[23] Carollo G, Garbujo A, Xin Q, Fabro J, Cool P, Canu P, et al. CuO/La0.5Sr0.5CoO3 nanocomposites in TWC. Appl Catal B Environ 2019;255:117753. https://doi.org/10.1016/j.apcatb.2019.117753.

[24] Brusamarello E, Blonda C, Salazar-Castro C, Canu P, Glisenti A. Industrially produced Fe- And Mn-based perovskites: effect of synthesis on reactivity in three-way catalysis: Part 2. ACS Omega 2021;6:24316–24. https://doi.org/10.1021/acsomega.1c02132.

[25] Perin G, Fabro J, Guiotto M, Xin Q, Natile MM, Cool P, et al. Cu@LaNiO3 based nanocomposites in TWC applications. Appl Catal B Environ 2017;209:214–27. https://doi.org/10.1016/j.apcatb.2017.02.064.

[26] Schön A, Dacquin JP, Granger P, Dujardin C. Non stoichiometric La1-yFeO3 perovskite-based catalysts as alternative to commercial three-way-catalysts? – impact of Cu and Rh doping. Appl Catal B Environ 2018;223:167–76. https://doi.org/10.1016/j.apcatb.2017.06.026.

[27] Russo N, Palmisano P, Fino D. Pd substitution effects on perovskite catalyst activity for methane emission control. Chem Eng J 2009;154:137–41. https://doi.org/10.1016/j.cej.2009.05.015.

[28] Wei X, Hug P, Figi R, Trottmann M, Weidenkaff A, Ferri D. Catalytic combustion of methane on nano-structured perovskite-type oxides fabricated by ultrasonic spray combustion. Appl Catal B 2010;94:27–37. https://doi.org/10.1016/j.apcatb.2009.10.017.

[29] Guo G, Lian K, Wang L, Gu F, Han D, Wang Z. High specific surface area $LaMO_3$ (M = Co, Mn) hollow spheres: synthesis, characterization and catalytic properties in methane combustion. RSC Adv 2014;4:58699–707. https://doi.org/10.1039/C4RA10053K.

[30] Najjar H, Batis H. Development of Mn-based perovskite materials: chemical structure and applications. Catal Rev Sci Eng 2016;58:371–438. https://doi.org/10.1080/01614940.2016.1198203.

[31] Hammami R, Ben AS, Batis H. Effects of thermal treatment on physico-chemical and catalytic properties of lanthanum manganite LaMnO3+y. Appl Catal A Gen 2009;353:145–53. https://doi.org/10.1016/j.apcata.2008.10.048.

[32] Mars P, van Krevelen DW. Oxidations carried out by means of vanadium oxide catalysts. Chem Eng Sci 1954;3:41–59. https://doi.org/10.1016/S0009-2509(54)80005-4.

[33] Alifanti M, Kirchnerova J, Delmon B, Klvana D. Methane and propane combustion over lanthanum transition-metal perovskites: Role of oxygen mobility. Appl Catal A Gen 2004;262:167–76. https://doi.org/10.1016/j.apcata.2003.11.024.

[34] Royer S, Alamdari H, Duprez D, Kaliaguine S. Oxygen storage capacity of La1−xA′xBO3 perovskites (with A′=Sr, Ce; B=Co, Mn)—relation with catalytic activity in the CH4 oxidation reaction. Appl Catal B 2005;58:273–88. https://doi.org/10.1016/j.apcatb.2004.12.010.

[35] Ponce S, Peña MA, Fierro JLG. Surface properties and catalytic performance in methane combustion of Sr-substituted lanthanum manganites. Appl Catal B Environ 2000;24:193–205. https://doi.org/10.1016/S0926-3373(99)00111-3.

[36] Spinicci R, Delmastro A, Ronchetti S, Tofanari A. Catalytic behaviour of stoichiometric and non-stoichiometric LaMnO3 perovskite towards methane combustion. Mater Chem Phys 2002;78:393–9. https://doi.org/10.1016/S0254-0584(02)00218-3.

[37] Najjar H, Lamonier J-F, Mentré O, Giraudon J-M, Batis H. Optimization of the combustion synthesis towards efficient LaMnO3+y catalysts in methane oxidation. Appl Catal B Environ 2011;106:149–59. https://doi.org/10.1016/j.apcatb.2011.05.019.

[38] Nakamura T, Misono M, Yoneda Y. Catalytic properties of perovskite-type mixed oxides, La 1–x Sr x CoO 3. Bull Chem Soc Jpn 1982;55:394–9. https://doi.org/10.1246/bcsj.55.394.

[39] Batis NH, Delichere P, Batis H. Physicochemical and catalytic properties in methane combustion of La1−xCaxMnO3±y ($0 \le x \le 1$; $-0.04 \le y \le 0.24$) perovskite-type oxide. Appl Catal A Gen 2005;282:173–80. https://doi.org/10.1016/j.apcata.2004.12.009.

[40] Esmaeilnejad-Ahranjani P, Khodadadi A, Ziaei-Azad H, Mortazavi Y. Effects of excess manganese in lanthanum manganite perovskite on lowering oxidation light-off temperature for automotive exhaust gas pollutants. Chem Eng J 2011;169:282–9. https://doi.org/10.1016/j.cej.2011.02.062.

[41] Schön A, Dujardin C, Dacquin J-P, Granger P. Enhancing catalytic activity of perovskite-based catalysts in three-way catalysis by surface composition optimisation. Catal Today 2015;258:543–8. https://doi.org/10.1016/j.cattod.2014.11.002.

[42] Xu Y, Dhainaut J, Dacquin JP, Lamonier JF, Zhang H, Royer S. On the role of cationic defects over the surface reactivity of manganite-based perovskites for low temperature catalytic oxidation of formaldehyde. Appl Catal B 2024;342. https://doi.org/10.1016/j.apcatb.2023.123400.

[43] Zhang C, Zeng K, Wang C, Liu X, Wu G, Wang Z, et al. LaMnO3 perovskites via a facile nickel substitution strategy for boosting propane combustion performance. Ceram Int 2020;46:6652–62. https://doi.org/10.1016/j.ceramint.2019.11.153.

[44] Esmaeilnejad-Ahranjani P, Khodadadi AA, Mortazavi Y. Self-regenerative function of Cu in LaMnCu0.1O3 catalyst: Towards noble metal-free intelligent perovskites for automotive exhaust gas treatment. Appl Catal A Gen 2020;602. https://doi.org/10.1016/j.apcata.2020.117702.

[45] Guo G, Lian K, Gu F, Han D, Wang Z. Three dimensionally ordered macroporous Pd-LaMnO3 self-regeneration catalysts for methane combustion. Chem Comm 2014;50:13575–7. https://doi.org/10.1039/c4cc05966b.

[46] Eyssler A, Mandaliev P, Winkler A, Hug P, Safonova O, Figi R, et al. The effect of the state of pd on methane combustion in Pd-Doped LaFeO 3. J Phys Chem C 2010;114:4584–94. https://doi.org/10.1021/jp911052s.

[47] Granger P, Renème Y, Lahougue A, Hamon C, Dhainaut F. Thermal aging of perovskite based natural gas vehicle catalysts: dependency of the mode of Pd incorporation. Top Catal 2020;63:1474–84. https://doi.org/10.1007/s11244-020-01331-x.

[48] Giebeler L, Kießling D, Wendt G. LaMnO3 perovskite supported noble metal catalysts for the total oxidation of methane. Chem Eng Technol 2007;30:889–94. https://doi.org/10.1002/ceat.200600306.

[49] Russo N, Palmisano P, Fino D. Pd-perovskite catalysts for methane emissions abatement: Study of Pd substitution effects. Top Catal 2009;52:2001–6. https://doi.org/10.1007/s11244-009-9382-2.

[50] Nishihata Y, Mizuki J, Tanaka H, Uenishi M, Kimura M. Self-regeneration of palladium-perovskite catalysts in modern automobiles. J Phys Chem Solids 2005;66-274-82. Doi: 10.1016/j.jpcs.2004.06.090.

[51] Steiger P, Delmelle R, Foppiano D, Holzer L, Heel A, Nachtegaal M, et al. Structural reversibility and nickel particle stability in lanthanum iron nickel perovskite-type catalysts. ChemSusChem 2017;10:2505–17. https://doi.org/10.1002/cssc.201700358.

[52] Neagu D, Tsekouras G, Miller DN, Ménard H, Irvine JTS. In situ growth of nanoparticles through control of non-stoichiometry. Nat Chem 2013;5:916–23. https://doi.org/10.1038/nchem.1773.

[53] Zheng Y, Marinova M, Granger P. Kinetics of methane combustion on model supported Pd/LaxMnO3 natural gas vehicle catalysts: Sensitivity of La-stoichiometry on the catalytic properties of Pd. Chem Eng J 2023;475:146389. https://doi.org/10.1016/j.cej.2023.146389.

[54] Chen J, Buchanan T, Walker EA, Toops TJ, Li Z, Kunal P, et al. Mechanistic understanding of methane combustion over Ni/CeO2: a combined experimental and theoretical approach. ACS Catal 2021;11:9345–54. https://doi.org/10.1021/acscatal.1c01088.

[55] Wang C, Xu Y, Tang J. Catalytic methane removal to mitigate its environmental effect. Sci China Chem 2023;66:1032–51. https://doi.org/10.1007/s11426-022-1487-8.

[56] Neagu D, Oh TS, Miller DN, Ménard H, Bukhari SM, Gamble SR, et al. Nano-socketed nickel particles with enhanced coking resistance grown in situ by redox exsolution. Nat Commun 2015;6.. https://doi.org/10.1038/ncomms9120.
[57] Guo X, Yin A, Dai W-L, Fan K. One pot synthesis of ultra-high copper contented Cu/SBA-15 material as excellent catalyst in the hydrogenation of dimethyl oxalate to ethylene glycol. Catal Letters 2009;132:22–7. https://doi.org/10.1007/s10562-009-0043-7.
[58] Osti A, Rizzato L, Cavazzani J, Glisenti A. Optimizing citrate combustion synthesis of A-site-deficient La, Mn-based perovskites: application for catalytic CH4 combustion in stoichiometric conditions. Catalysts 2023;13:1177. https://doi.org/10.3390/catal13081177.
[59] Shannon RD. Revised effective ionic radii and systematic studies of interatomie distances in halides and chaleogenides. Acta Cryst 1976;32:751–67. https://doi.org/10.1107/S0567739476001551.
[60] Wei T, Jia L, Zheng H, Chi B, Pu J, Li J. LaMnO3-based perovskite with in-situ exsolved Ni nanoparticles: a highly active, performance stable and coking resistant catalyst for CO2 dry reforming of CH4. Appl Catal A Gen 2018;564:199–207. https://doi.org/10.1016/j.apcata.2018.07.031.
[61] Patcas F, Buciuman FC, Zsako J. Oxygen non-stoichiometry and reducibility of B-site substituted lanthanum manganites. Termochim Acta 2020;360:71–6. https://doi.org/10.1016/S0040-6031(00)00532-3.
[62] Chen J, Shen M, Wang X, Qi G, Wang J, Li W. The influence of nonstoichiometry on LaMnO3 perovskite for catalytic NO oxidation. Appl Catal B 2013;134–135:251–7. https://doi.org/10.1016/j.apcatb.2013.01.027.
[63] Carbon XPS Periodic Table. Thermo Fisher Scientific, https://www.thermofisher.com/it/en/home/materials-science/learning-center/periodic-table/non-metal/carbon.html [accessed 12 March 2024].
[64] Bauschlicher CW, Jacobson NS, Myers DL, Opila EJ. Computational chemistry derivation of Cr, Mn, and La hydroxide and oxyhydroxide thermodynamics. J Phys Chem A 2022;126:1551–61. https://doi.org/10.1021/acs.jpca.2c00764.
[65] Fleming P, Farrell RA, Holmes JD, Morris MA. The rapid formation of $La(OH)_3$ from La_2O_3 powders on exposureto water vapor. J Am Ceram Soc 2010;93:1187–94. https://doi.org/10.1111/j.1551-2916.2009.03564.x.
[66] Taguchi H, Matsu-ura S, Nagao M, Choso T, Tabata K. Synthesis of LaMnO3 by firing gels using citric acid. J Solid State Chem 1997;129:60–5. https://doi.org/10.1006/jssc.1996.7229.
[67] Sihaib Z, Puleo F, Pantaleo G, La Parola V, Valverde JL, Gil S, et al. The effect of citric acid concentration on the properties of LaMnO3 as a catalyst for hydrocarbon oxidation. Catalysts 2019;9. https://doi.org/10.3390/catal9030226.
[68] Biesinger MC, Payne BP, Grosvenor AP, Lau LWM, Gerson AR, Smart RSC. Resolving surface chemical states in XPS analysis of first row transition metals, oxides and hydroxides: Cr, Mn, Fe, Co and Ni. Appl Surf Sci 2011;257:2717–30. https://doi.org/10.1016/j.apsusc.2010.10.051.
[69] San Choi J, Ahn CW, Bae JS, Kim TH. Identifying a perovskite phase in rare-earth nickelates using X-ray photoelectron spectroscopy. Curr Appl Phys 2020;20:102–5. https://doi.org/10.1016/j.cap.2019.10.013.
[70] Osti A, Rizzato L, Cavazzani J, Meneghello A, Glisenti A. Perovskite oxide catalysts for enhanced CO_2 reduction: embroidering surface decoration with Ni and Cu nanoparticles. Catalysts 2024;14. https://doi.org/10.3390/catal14050313.
[71] Zaza F, Luisetto I, Serra E, Tuti S, Pasquali M. Catalytic combustion of methane by perovskite-type oxide nanoparticles as pollution prevention strategy. AIP Conf Proc 2016;1749:020003. https://doi.org/10.1063/1.4954486.